

This item is likely protected under Title 17 of the U.S. Copyright Law. Unless on a Creative Commons license, for uses protected by Copyright Law, contact the copyright holder or the author.

Access to this work was provided by the University of Maryland, Baltimore County (UMBC) ScholarWorks@UMBC digital repository on the Maryland Shared Open Access (MD-SOAR) platform.

Please provide feedback

Please support the ScholarWorks@UMBC repository by emailing scholarworks-group@umbc.edu and telling us what having access to this work means to you and why it's important to you. Thank you.

PROBING THE MYSTERIES OF THE X-RAY BINARY 4U 1210-64 WITH ASM, PCA, MAXI, BAT, AND *SUZAKU*

JOEL B. COLEY^{1,2}, ROBIN H. D. CORBET^{1,2}, KOJI MUKAI^{1,2}, AND KATJA POTTSCHMIDT^{1,3}

¹ University of Maryland Baltimore County, 1000 Hilltop Cir, Baltimore, MD 21250 USA; jcoley1@umbc.edu

² CRESST/Mail Code 662, X-ray Astrophysics Laboratory, NASA Goddard Space Flight Center, Greenbelt, MD 20771, USA

³ CRESST/Mail Code 661, X-ray Astroparticle Physics Laboratory, NASA Goddard Space Flight Center, Greenbelt, MD 20771, USA

Received 2013 December 19; accepted 2014 July 24; published 2014 September 9

ABSTRACT

4U 1210-64 has been postulated to be a high-mass X-ray binary powered by the Be mechanism. X-ray observations with *Suzaku*, the *ISS* Monitor of All-sky X-ray Image (MAXI), and the *Rossi X-ray Timing Explorer* Proportional Counter Array (PCA) and All Sky Monitor (ASM) provide detailed temporal and spectral information on this poorly understood source. Long-term ASM and MAXI observations show distinct high and low states and the presence of a 6.7101 ± 0.0005 day modulation, interpreted as the orbital period. Folded light curves reveal a sharp dip, interpreted as an eclipse. To determine the nature of the mass donor, the predicted eclipse half-angle was calculated as a function of inclination angle for several stellar spectral types. The eclipse half-angle is not consistent with a mass donor of spectral type B5 V; however, stars with spectral types B0 V or B0-5 III are possible. The best-fit spectral model consists of a power law with index $\Gamma = 1.85^{+0.04}_{-0.05}$ and a high-energy cutoff at 5.5 ± 0.2 keV modified by an absorber that fully covers the source as well as partially covering absorption. Emission lines from S XVI K α , Fe K α , Fe XXV K α , and Fe XXVI K α were observed in the *Suzaku* spectra. Out of eclipse, the Fe K α line flux was strongly correlated with unabsorbed continuum flux, indicating that the Fe I emission is the result of fluorescence of cold dense material near the compact object. The Fe I feature is not detected during eclipse, further supporting an origin close to the compact object.

Key words: stars: individual (4U 1210-64) – stars: neutron – X-rays: stars

Online-only material: color figures

1. INTRODUCTION

4U 1210-64 is an unusual X-ray binary (XRB) first detected by the *Uhuru* satellite in 1978 (Forman et al. 1978). Forman et al. (1978) found that 4U 1210-64 appears to be a variable source with a mean flux of 8.9×10^{-11} erg cm⁻² s⁻¹ in the 2–6 keV band. Subsequent detections of 4U 1210-64 include the *Einstein* (Elvis et al. 1992) and *EXOSAT* (Reynolds et al. 1999) slew surveys at fluxes 1.7×10^{-11} erg cm⁻² s⁻¹ and $\sim 7 \times 10^{-10}$ erg cm⁻² s⁻¹ in the 0.16–3.5 keV and 1–8 keV bands, respectively; the wide-field cameras (WFC) on board *BeppoSAX* (Verrecchia et al. 2007), *INTEGRAL*/IBIS (Ubertini et al. 2003) and the Burst Alert Telescope (BAT) on board the *Swift* observatory (Tueller et al. 2010; Cusumano et al. 2010) at fluxes 2.57×10^{-10} erg cm⁻² s⁻¹, 1.1×10^{-11} erg cm⁻² s⁻¹, and $\sim 2 \times 10^{-11}$ erg cm⁻² s⁻¹ in the 2–10 keV, 20–100 keV, and 14–195 keV bands, respectively.

A soft X-ray counterpart at coordinates (J2000) R.A. = 12:13:14.7, decl. = –64:52:31 with a position uncertainty of $\sim 4''$ was revealed (Revnivtsev et al. 2007) in observations conducted with the X-Ray Telescope (XRT; Burrows et al. 2005) on board *Swift*. Revnivtsev et al. (2007) modeled the X-ray spectrum of 4U 1210-64 using a continuum consisting of a power law with a hard photon index and an emission feature at 6.7 keV with an equivalent width (EQW) of ~ 400 eV. These observations resulted in the classification of 4U 1210-64 as an intermediate polar cataclysmic variable (CV; Revnivtsev et al. 2007).

Observations using the *Swift*/XRT in late 2006 and early 2008 confirmed the presence of an emission feature at 6.7 keV, thought to be Fe XXV (Masetti et al. 2010). The emission feature, observed to be prominent when the source is at intermediate flux levels, was not seen when the source entered periods of

low or high flux (Masetti et al. 2010). At intermediate flux levels, the EQW of the emission line was observed to be ~ 1.6 keV. This very large EQW is suggestive of a blend of Fe lines. While Revnivtsev et al. (2007) suggested that the spectral properties indicate that 4U 1210-64 is a CV, Masetti et al. (2010) proposed that the stellar remnant in the system is a neutron star based on the very large EQW and variability of the emission feature. Under the assumption of a power-law continuum and a distance of ~ 2.8 kpc (Masetti et al. 2009), the high state X-ray luminosity of 4U 1210-64 was found to be 1.9×10^{35} erg s⁻¹ in the 2–10 keV band (Masetti et al. 2010). This exceeds the typical luminosities observed in CVs by a factor of ~ 1 –2 orders of magnitude (Barlow et al. 2006; Revnivtsev et al. 2008; Brunschweiler et al. 2009). A blackbody soft excess with a temperature of ~ 1.5 keV was found in 4U 1210-64, which implies that the accretor is more compact than a white dwarf (Masetti et al. 2010). Masetti et al. (2010) concluded that the presence of the soft excess provides compelling evidence against a CV interpretation of the system.

The optical counterpart of 4U 1210-64 was observed on MJD 54529.3 using the 1.5 m Cerro Tololo Interamerican Observatory (CTIO) in Chile (Masetti et al. 2009). Based on its optical spectrum, Masetti et al. (2009) proposed that the spectral class of the mass donor is B5 V. The features observed in the optical spectrum consist of Balmer series lines in absorption and emission of neutral helium, singly ionized helium, and a blend of doubly ionized nitrogen and carbon. The EQW of the H α line was observed to be approximately 2.5 Å (Masetti et al. 2009). This is less than half the expected value for a B5 V star, which suggests that emission features are present. While an early-type mass donor suggests that 4U 1210-64 is a high-mass X-ray binary (HMXB), the presence of a B5 V main-sequence star in an HMXB would be unprecedented (Negueruela 1998).

The majority of Be X-ray binaries (BeXBs) host primaries with spectral properties that range from late O to early B type stars. This will be discussed in further detail in Section 4.

A 6.7 day orbital period was discovered using data from the *Rossi X-ray Timing Explorer* All-Sky Monitor (ASM; Corbet & Mukai 2008). In addition, Corbet & Mukai (2008) report three main states of the system along with the possibility of an eclipse. We investigate these results in more detail in Section 3.1 using additional data from ASM, the Monitor of All-Sky X-ray Image (MAXI) on board the *International Space Station* (ISS) and Burst Alert Telescope (BAT) instruments on board the *Swift* spacecraft.

This paper is structured in the following order: *Suzaku*, MAXI, PCA, and ASM observations are presented in Section 2, Section 3 focuses on the results of the X-ray campaign, and Section 4 presents a discussion of the results. The conclusions are outlined in Section 5. If not stated otherwise, the uncertainties and limits presented in the paper are at the 1σ confidence level.

2. OBSERVATIONS AND DATA ANALYSIS

The observations outlined below consist of data collected during a two-day *Suzaku* observation of 4U 1210-64 (2010 December 23–25), pointed observations using the *RXTE* Proportional Counter Array (PCA) as well as long-term observations of the system using the following all-sky monitors: MAXI, ASM, and BAT.

2.1. RXTE

2.1.1. ASM

The ASM on board *RXTE* (Levine et al. 1996) consisted of three coded-aperture Scanning Shadow Cameras, each containing a position-sensitive proportional counter (PSPC) with a field of view (FOV) of $6^\circ \times 90^\circ$ FWHM (Remillard & Levine 1997). ASM scanned approximately 80% of the sky per spacecraft orbit (~ 90 minutes) with a 90 s time resolution (“dwell”) (Remillard & Levine 1997; Levine et al. 1996). The FOV of the cameras is fixed on the sky for the duration of a “dwell.” Sensitive to energies in the 1.5–12 keV band, ASM observed 4U 1210-64 from MJD 50087 to 55924.

The light curves were retrieved from the ASM/*RXTE* database⁴ managed by MIT, which includes “dwell-by-dwell” light curves and daily averaged light curves. The light curves are divided into three energy bands: 1.5–3 keV, 3–5 keV, and 5–12 keV. Over the entire energy range (1.5–12 keV), the Crab produces approximately $75.5 \text{ counts s}^{-1}$ (Remillard & Levine 1997; Levine et al. 1996). “Blank field” observations of regions at high Galactic latitudes indicate that a systematic uncertainty of $\sim 0.1 \text{ counts s}^{-1}$ must be taken into account (Remillard & Levine 1997; Levine et al. 1996). We used the “dwell-by-dwell” light curves in our analysis (see Section 3.1).

2.1.2. PCA

Consisting of five proportional counter units (PCUs), the PCA was sensitive to X-rays in the energy band of 2–60 keV. The total effective area of the instrument was $\sim 6500 \text{ cm}^2$ with an FOV at FWHM of 1° (Jahoda et al. 1996). At 6.0 keV, the energy resolution FWHM in the PCA is $\sim 1 \text{ keV}$ (Jahoda et al. 2006).

4U 1210-64 was observed 65 times between MJD 54804.0–54842.0. Individual observations typically lasted for 2–4 ks

but were as short as 1.4 ks and as long as 45.6 ks. Data set IDs were 93455-01 (23 observations) and 94409-01 (42 observations). The majority of the observations were performed during a single spacecraft orbit with no interruptions; longer ones spanned multiple orbits, with interruptions due to Earth occultations and/or SAA passages. Of the five PCUs, only PCU2 was used consistently for these observations; thus, we have opted to analyze only data taken with PCU2. The Crab produces $\sim 2000\text{--}2400 \text{ counts s}^{-1}$ in the PCU2 top layer.⁵

Each detected event was recorded in different ways by the on-board experiment data system (EDS). We analyzed Standard2 mode data, producing 129-channel spectra every 16 s, for spectral analysis and for low-frequency timing analysis. We generated the “faint” model background,⁶ since the source mostly stayed below $40 \text{ counts s}^{-1} \text{ PCU}^{-1}$. For high-frequency timing analysis, we generated light curves in 10 ms bins using the GoodXenon event mode data, without background subtraction. Spectral data including background subtraction were reduced and analyzed using the standard screening criteria (Jahoda et al. 2006).

2.2. MAXI

The MAXI instrument is an X-ray slit camera sensitive to photons in the energy range 0.5–30 keV (Matsuoka et al. 2010). MAXI consists of two types of slit cameras, the Gas Slit Camera and the Solid-state Slit Camera, which observe the X-ray variability of over 1000 sources over every ISS orbit of approximately 92 minutes (Matsuoka et al. 2010). Of the two cameras, we make use of the GSC data that are routinely made available by the MAXI team.

Covering an energy range of 2–30 keV, the GSC consists of 12 one-dimensional PSPC, which make six camera units (Matsuoka et al. 2010). The overall FOV is a $160^\circ \times 3^\circ$ slit, which scans both the horizon and zenith directions (Matsuoka et al. 2010).

We analyzed MAXI data obtained between MJD 55061.5–56394.5. Light curves of energies 2–4 keV, 4–10 keV, and 10–20 keV were retrieved from the data available in the MAXI RIKEN database.⁷ The 2–4 keV and 4–10 keV light curves were subsequently co-added for comparison with the light curves produced by the ASM.

2.3. Swift

The BAT on board the *Swift* spacecraft is a hard XRT operating in the 15–150 keV energy band (Barthelmy et al. 2005). The detector is composed of CdZnTe where the detecting area and FOV are 5240 cm^2 and 1.4 sr (half-coded), respectively (Barthelmy et al. 2005). The BAT provides an all-sky hard X-ray survey with a sensitivity of $\sim 2 \text{ mCrab}$ (Barthelmy et al. 2005). The Crab produces $\sim 0.045 \text{ counts s}^{-1}$ over the 14–195 keV energy band.

We analyzed BAT data obtained during the time period MJD 55152–56141. Light curves were retrieved using Krimm et al.’s (2013) extraction of the BAT data available on the NASA GSFC HEASARC Web site,⁸ which includes orbital and daily averaged light curves. We used the orbital light curves in the 15–50 keV energy band in our analysis (see Section 3).

⁴ http://xte.mit.edu/ASM_lc.html

⁵ <http://www.sternwarte.uni-erlangen.de/~wilms/rxte/>

⁶ <http://heasarc.nasa.gov/docs/xte/recipes/pcbackest.html>

⁷ <http://maxi.riken.jp/top/>

⁸ <http://heasarc.gsfc.nasa.gov/docs/swift/results/transients/>

2.4. *Suzaku*

The *Suzaku* observation of 4U 1210-64 took place in 2010 December 23–25 (MJD 55553.16–55555.15) with an exposure time of ~ 80 ks (ObsID 405045010). Data, collected using the X-ray Imaging Spectrometer (XIS) and Hard X-ray Detector (HXD) instruments, were reduced and analyzed using the standard criteria defined in the ABC Guide.⁹ These procedures are described below.

2.4.1. XIS data

The *Suzaku* XIS suite consists of four X-ray imaging telescopes each fitted with a CCD chip covering a region of 17.8×17.8 (Koyama et al. 2007; Mitsuda et al. 2007). Three of the chips are front-illuminated: XIS0, XIS2, and XIS3. The energy resolution FWHM in the front-illuminated XIS instruments is ~ 130 eV at 6.0 keV. Sensitive to X-rays ranging from 0.6 to 10 keV, the effective area of the front-illuminated XIS instruments is 330 cm^2 at 1.5 keV. XIS2 failed in late 2006 due to a charge leak. The back-illuminated XIS instrument, XIS1, is characterized by a greater sensitivity to X-rays in the energy band between 0.2–6 keV.

4U 1210-64 was observed in full window mode with a data readout of 8 s. Data collected using the XIS were reduced and screened using the HEASoft v.6.13 package and calibration files dated 2013 September 8 (XIS) and 2011 June 30 (XRT) implementing the procedures defined in the *Suzaku* ABC Guide. The data were reprocessed with the FTOOL *aepipeline* using the standard criteria to apply the newest calibration and default screening criteria. The XIS exposures in the 3×3 and 5×5 event modes were combined using XSELECT. Circular regions of radius $3.9'$ centered on the source and offset from the source were selected to distinguish between photons originating from the source and those originating from the background. The light curves were binned at 16 s.

Response matrices were generated using the *xismfgen* and *xissimarfgen* FTOOL packages. Pileup was taken into consideration in the region files, where the central pixels were shown to be affected. As a result, the inner parts of the point-spread function were removed using two overlapping rectangular shaped regions to reduce pile-up to $\lesssim 1\%$ using the FTOOLS *aeattcor2* and *pileest*. *Aeattcor2* creates an improved attitude file, which is then applied to the event file. The FTOOL *pileest* was then used on the improved event file, which provides a rough estimate of the degree of pile-up.

Data in the spectral file produced by XSELECT were further processed using the FTOOL *GRPPHA*. *GRPPHA* is designed to define the binning, quality flags and systematic errors of the spectra and used the bad quality flag to further eliminate bad data from the PHA file. Bins were grouped to ensure a minimum of 20 counts in each in the XIS spectra. The spectrum was analyzed using XSPEC v12.7.1d. To avoid poorly calibrated Si and Au features, only the energy ranges of 0.5–1.7 keV and 2.1–9.2 keV were considered (Nowak et al. 2011). We will discuss the spectral analysis and results in Section 3.4.

2.4.2. HXD data

The HXD is a non-imaging X-ray spectrometer consisting of 64 silicon PIN diodes as well as the Gadolinium silicate crystal (GSO) instruments (Mitsuda et al. 2007). Our analysis only considers data collected by the PIN diodes because 4U 1210-64

is not bright enough for GSO analysis. The calibration files used in the analysis of the HXD data were dated 2010 December 6.

The HXD-PIN consists of 16 identical (4×4) detector units surrounded by 20 anti-coincidence counters. The usable energy range for the HXD PIN diodes is between 15 and 70 keV (Mitsuda et al. 2007; Takahashi et al. 2007). The effective area of the HXD instrument is $\sim 160 \text{ cm}^2$ at 20 keV (Mitsuda et al. 2007; Takahashi et al. 2007). For this specific observation, 4U 1210-64 is not easily detectable at energies exceeding ~ 30 keV. As a result, the analyzed part of the spectrum is between 15–30 keV.

The HXD-PIN spectral data were extracted and reduced using the “cleaned” event files in the *hxd/event_c1* directory and the *hxdpinxbpi* FTOOL package, respectively. The FTOOL *hxdpinxbpi* automatically runs the tasks outlined as follows. Good time intervals were calculated using the Non X-ray Background (NXB)¹⁰ data overlapping in time with the GTI of the observation. The source and NXB spectra are extracted using *hxdpinxbpi*. The rate in the NXB event file is scaled by a factor of 10 to account for Poisson errors. As a result, the exposure time of the derived background spectra and light curves must be increased by a factor of 10. Since the NXB spectrum does not include the Cosmic X-ray Background (CXB), a simulated CXB spectrum was produced using the parameters determined by Boldt (1987). The total PIN background spectrum is the sum of the NXB and simulated CXB spectra, which were added together using *addspec*. The net count rates for the NXB and CXB spectra are 0.2336 ± 0.0006 and $0.0153 \pm 0.0001 \text{ counts s}^{-1}$, respectively. The source spectrum is dead time corrected by $\sim 4\%$ – 5% .

3. RESULTS

3.1. Long-term Temporal Analysis

Using data acquired from the ASM, MAXI, and BAT instruments, we produced light curves of 4U 1210-64 to investigate long-term variability of the source (see Figure 1). Data produced by ASM, MAXI, and BAT span periods of ~ 16 yr, ~ 3.3 yr, and ~ 5 yr, respectively.

3.1.1. ASM Temporal Analysis

Three distinct states of the system, two active phases and a quiescent phase, are seen in the ASM light curve (see Figure 1, bottom). To parameterize the states observed in the system, the light curve was fit using an asymmetric “step-and-ramp” function (see Figure 1, bottom). The parameters in this model are as follows: the times corresponding to the start of the transition between the first active state to the quiescent state, T_1 , the start of the transition between the quiescent state and the second active state, T_2 , the transition time between state 1 and state 2, ΔT_1 , the transition time between state 2 and state 3, ΔT_2 , the count rates during both active states, C_{act1} and C_{act2} , and the count rate during the quiescent state, C_{quies} . The model parameters are reported in Table 1. The duration of the quiescent phase was found to be 2506^{+36}_{-26} days ($6.19^{+0.10}_{-0.07}$ yr) using the following equation:

$$\Delta T_{\text{quies}} = T_2 - (T_1 + \Delta T_1). \quad (1)$$

A power spectrum was used to search for periodicities in temporal data (Scargle 1982; Corbet & Mukai 2008). Power spectra, produced using the MAXI and ASM light curves at a time resolution of one dwell (90 s), show the presence of a 6.7101 ± 0.0005 day peak (see Figure 2, bottom).

⁹ <http://heasarc.gsfc.nasa.gov/docs/suzaku/analysis/abc/>

¹⁰ ftp://legacy.gsfc.nasa.gov/suzaku/data/background/pinnxb_ver2.0_tuned/

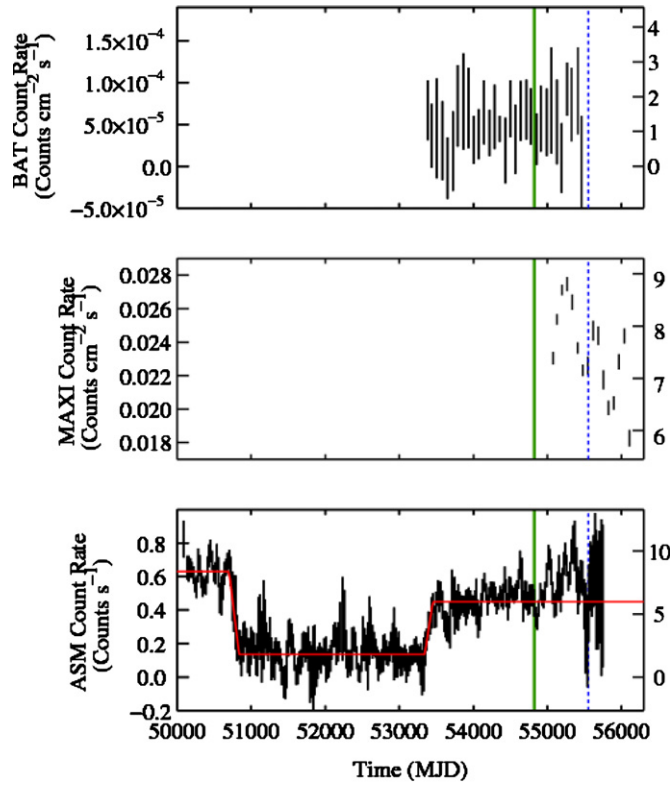


Figure 1. Long-term light curves of 4U 1210-64 produced by BAT in the 15–150 keV band (top), MAXI in the 2–10 keV band (middle), and ASM in the 1.5–12 keV band (bottom) show a two-year time overlap between ASM and MAXI and a five-year time overlap between ASM and BAT. The ASM, MAXI, and BAT light curves use 21 day, 70 day, and 70 day time bins, respectively. The times of the PCA and *Suzaku* observations are indicated by the green shaded region and blue dashed line, respectively. The ASM light curve (bottom) is fit with an asymmetric “step and ramp” function (solid red line), which models the long-term behavior of the system.

(A color version of this figure is available in the online journal.)

Best-fit Parameters for the States Observed in 4U 1210-64	
Model Parameter	ASM
T_1 (MJD)	50703^{+13}_{-5}
ΔT_1 (days)	135^{+32}_{-22}
$T_1 + \Delta T_1$ (MJD)	50838^{+35}_{-22}
$C_{\text{act}1}$ (counts s $^{-1}$)	0.63 ± 0.02
$C_{\text{act}2}$ (counts s $^{-1}$)	$0.45^{+0.02}_{-0.01}$
T_2 (MJD)	53444^{+11}_{-13}
ΔT_2 (days)	109^{+16}_{-21}
$T_2 + \Delta T_2$ (MJD)	53452^{+19}_{-25}
C_{quies} (counts s $^{-1}$)	0.136 ± 0.009
ΔT_{quies} (days)	2506^{+36}_{-26}
χ^2_{ν} (dof)	1.19 (222)

The false-alarm probability (FAP; Scargle 1982) in the ASM light curve is $\sim 10^{-9}$. We interpret this peak as the orbital period of the system.

For this paper, we use an ephemeris based on the orbital period observed in the power spectrum (see Figure 3, bottom) and time of mid-eclipse: $P = 6.7101 \pm 0.0005$ days and $T_0 = \text{MJD } 5553.098 \pm 0.002$. To parameterize the orbital modulation of the system, the “dwell-by-dwell” ASM light curves were folded using the orbital period.

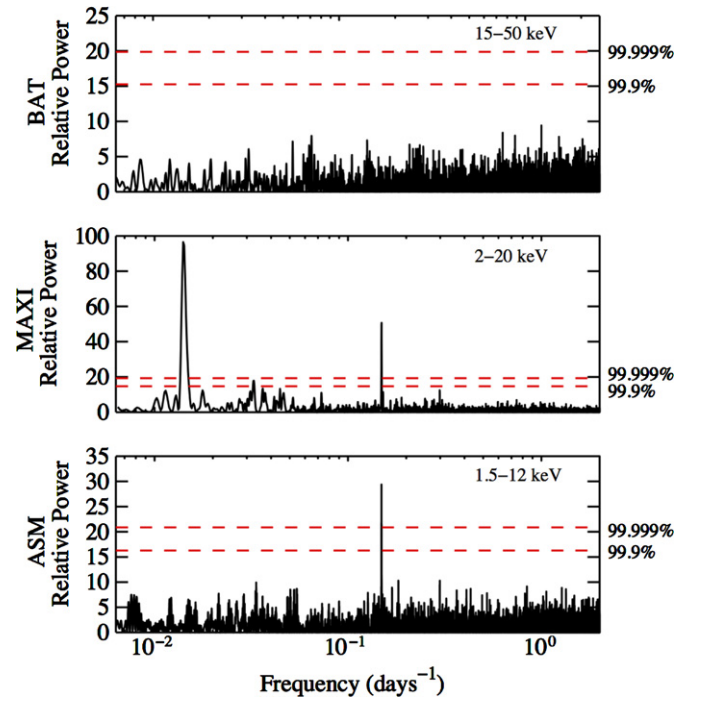


Figure 2. Power spectra produced by BAT (top), MAXI (middle), and ASM (bottom) with the 99.9% and 99.999% confidence intervals shown. The BAT (top), MAXI (middle), and ASM (bottom) data are in the 15–50 keV, 2–20 keV, and 1.5–12 keV bands, respectively. The ~ 70 day precession period of the ISS is also seen in the MAXI power spectrum.

(A color version of this figure is available in the online journal.)

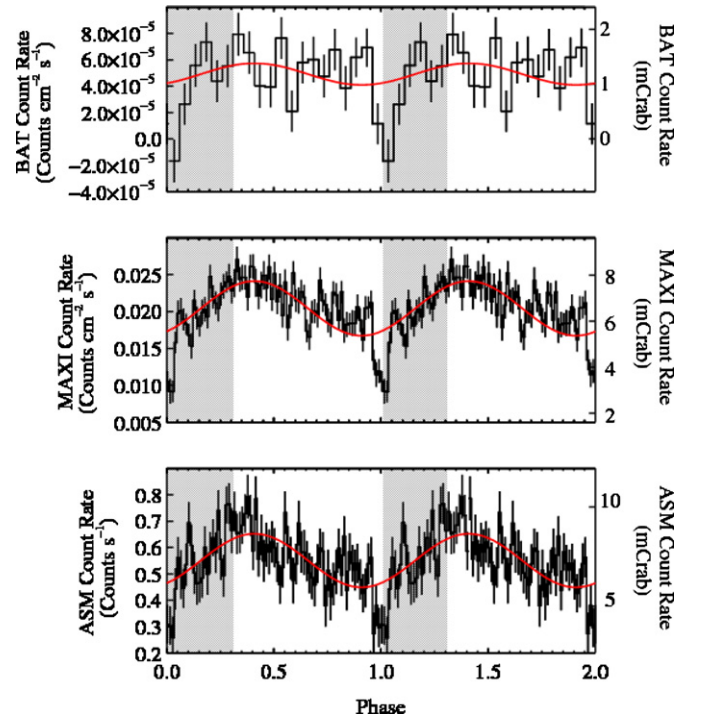


Figure 3. BAT (top), MAXI (middle), and ASM (bottom) light curves folded on the orbital period using 20 bins (BAT) and 80 bins (ASM and MAXI). The shaded region indicates the orbital phases of the system for the duration of the *Suzaku* observation. The sharp dip in flux between phases $\phi \sim -0.04$ and $\phi \sim 0.03$ is interpreted as an eclipse. The solid red line is the sinusoidal fit to the folded light curves using the ephemeris defined in Section 3.1.1.

(A color version of this figure is available in the online journal.)

Table 2
4U 1210-64 Eclipse Model Parameters

Model Parameter	ASM (1.5–12 keV)	MAXI (2–20 keV)	Combined	BAT ^a (15–50 keV)
ϕ_{ing}	$-0.047^{+0.004}_{-0.003}$	-0.044 ± 0.002	-0.045 ± 0.002	...
$\Delta\phi$	$0.014^{+0.001}_{-0.006}$	0.013 ± 0.002	$0.014^{+0.001}_{-0.002}$...
C	0.54 ± 0.01^b	1.97 ± 0.03^c	...	5.5 ± 0.4^d
ϕ_{egr}	0.033 ± 0.005	0.031 ± 0.002	0.031 ± 0.002	...
C_{ecl}	$0.34^{+0.02}_{-0.03}^b$	1.11 ± 0.07^c	...	1.0 ± 1.4^d
$\Delta\phi_{\text{ecl}}$	$0.066^{+0.007}_{-0.008}$	0.062 ± 0.004	0.062 ± 0.003	...
T_{mid}^e	55553.099 ± 0.004	55553.098 ± 0.002	55553.098 ± 0.002	...
Θ_e^f	$11.9^{+1.3}_{-1.5}$	$11.1^{+0.6}_{-0.7}$	11.2 ± 0.6	...
χ^2_{ν} (dof)	0.92(146)	1.21(84)	...	0.93(96)

Notes.

^a The ϕ_{ing} , $\Delta\phi$, ϕ_{egr} parameters in the BAT fit are frozen to the weighted average of the ASM and MAXI values.

^b Units are counts s^{-1} .

^c Units are 10^{-2} counts $\text{cm}^{-2} \text{s}^{-1}$.

^d Units are 10^{-5} counts $\text{cm}^{-2} \text{s}^{-1}$.

^e Units are MJD.

^f Units are degrees.

3.1.2. MAXI Temporal Analysis

We confirmed the orbital period using MAXI. We folded the MAXI light curve over the orbital period using the ephemeris described above (see Figure 3, middle), showing that the binned folded light curve strongly agrees with that produced by ASM. Compared to the ASM power spectrum, more statistical noise is apparent in the power spectrum produced using MAXI data (see Figure 2, middle). A “blind search” for the period of the system yields an FAP of $\sim 10^{-3}$. Considering only the period derived by the ASM data, a single trial search, the FAP is reduced to $\sim 10^{-6}$.

3.1.3. BAT Temporal Analysis

The modulation interpreted as the 6.7 day orbital period was not detected in the power spectrum produced by the BAT instrument (see Figure 2, top). Comparisons between the BAT power spectrum and ASM power spectrum indicate that BAT does not have the sensitivity to detect the 6.7 day modulation at the level seen in ASM and MAXI, respectively (see Figure 2, top). We define the modulation depth as $(\text{Count}_{\text{max}} - \text{Count}_{\text{min}})/\text{MeanCount}$.

We folded the BAT light curve on the orbital period using the ephemeris defined by the ASM (see Section 3.1.1 and Figure 3, top), showing that the binned folded light curve is consistent with that produced by ASM and MAXI with a possible indication of an eclipse centered at $\phi = 0$.

3.2. Eclipse Profile

The folded light curves show the presence of a sharp dip between orbital phases $\phi \sim -0.04$ and $\phi \sim 0.03$, which is suggestive of an eclipse. The source emission does not reach zero counts s^{-1} . We interpret this dip as an eclipse since the feature is persistent over many years of data. The feature is seen at the same orbital phase in States 1 and 3 (see Table 1), which are separated by $\gtrsim 6$ yr. The rapid ingress and egress requires obscuration by clearly defined boundaries that are suggestive of an object such as the mass donor in the system.

The eclipse was modeled using a symmetric “step and ramp” function (see Figure 4) where the intensities are assumed to remain constant before ingress, during eclipse, and after

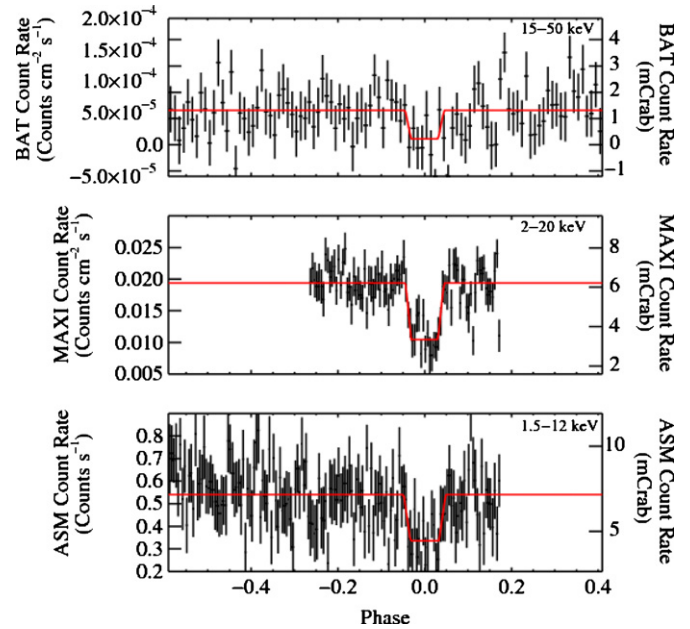


Figure 4. BAT (top), MAXI (middle), and ASM (bottom) folded light curves are fit with a symmetric “step and ramp” function, which models the eclipse. The BAT (top), MAXI (middle), and ASM (bottom) data are in the 15–50 keV, 2–20 keV, and 1.5–12 keV bands, respectively.

(A color version of this figure is available in the online journal.)

egress and follow a linear trend during the ingress and egress transitions. The parameters in this model are as follows: the phases corresponding to the start of ingress as well as egress, ϕ_{ing} and ϕ_{egr} , the duration of ingress and egress, $\Delta\phi$, the count rates before ingress and after egress, C , and the count rate during eclipse, C_{ecl} . The symmetric nature of the model ensures that the duration of ingress and egress, $\Delta\phi$, as well as the count rate before ingress and after egress, C , are equal. The eclipse model parameters are reported in Table 2. The eclipse duration and mid-eclipse are calculated using Equations (2) and (3).

$$\Delta\phi_{\text{ecl}} = \phi_{\text{egr}} - (\phi_{\text{ing}} + \Delta\phi) \quad (2)$$

$$\phi_{\text{mid}} = \frac{1}{2}(\phi_{\text{egr}} + (\phi_{\text{ing}} + \Delta\phi)). \quad (3)$$

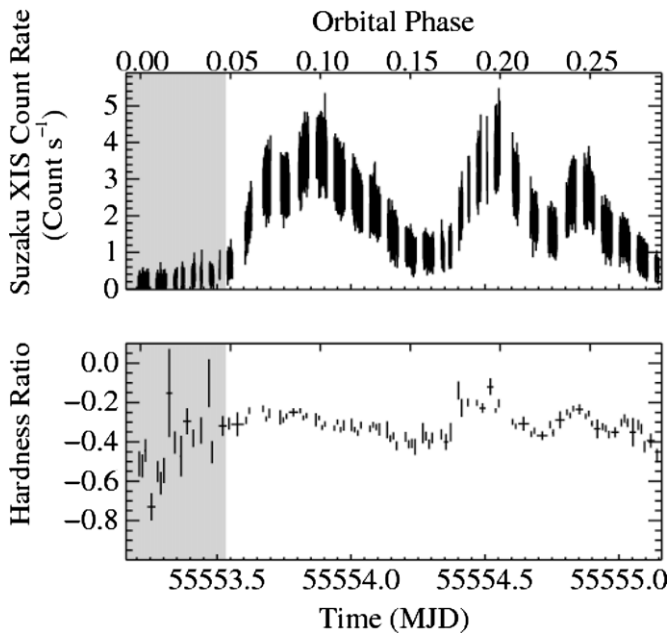


Figure 5. Weighted average of the *Suzaku* XIS0 and XIS3 light curves using bin sizes of 16 s (top). The top axis indicates the orbital phase of the system. The shaded region indicates the egress start and end times calculated by the “step-and-ramp” function. The hardness ratio (bottom), which uses bin sizes of 1000 s, is defined as $(C_{\text{hard}} - C_{\text{soft}})/(C_{\text{hard}} + C_{\text{soft}})$, where the soft and hard energy bands are 0.5–4 keV and 4–10 keV, respectively.

Since the *Suzaku* observation begins at MJD 55553.1, we express the time of mid-eclipse, T_{mid} , at an epoch closest to the *Suzaku* observation (see Table 2). The eclipse duration, time of mid-eclipse, and eclipse half-angle ($\Delta\phi_{\text{ecl}} \times 180^\circ$) from fitting the ASM and MAXI folded light curves are reported in Table 2. The fits of both the ASM and MAXI data, which use 150 and 88 bins, respectively, indicate that the mid-eclipse times and eclipse durations are in agreement at the 1σ level. While all model parameters were free for the ASM and MAXI fits, the phases corresponding to the start of ingress as well as egress and the transition duration in the BAT fit, which uses 96 bins, were frozen to the weighted average of the ASM and MAXI values.

3.3. Short-term Temporal Analysis

3.3.1. *Suzaku*

The two-day *Suzaku* observation in 2010 December took place during the phase of transition from the minimum to the maximum of the 6.7 day modulation (see Figure 3). We binned the *Suzaku* light curves to a resolution of 16 s to investigate short-term variability in the system, shown in the light curve produced by the sum of the XIS0 and XIS3 light curves (see Figure 5).

The two-day *Suzaku* observation revealed large variations in flux indicative of significant variability beyond the orbital modulation. The modulation depth between the peak in the light curve and the mean count rate is of the order of 140%.

We divided the light curve into two energy bands where the soft band is defined between energies of 0.5–4 keV, characterized by the count rate C_{soft} , and the hard band is between 4–10 keV, characterized by the count rate C_{hard} . Using the definition in Equation (4), we produced a hardness ratio (see Figure 5, bottom) binned to a resolution of ~ 1000 s, where a soft spectrum is indicated by negative values and a hard spectrum is indicated by positive values. The hardness ratio was also plotted against

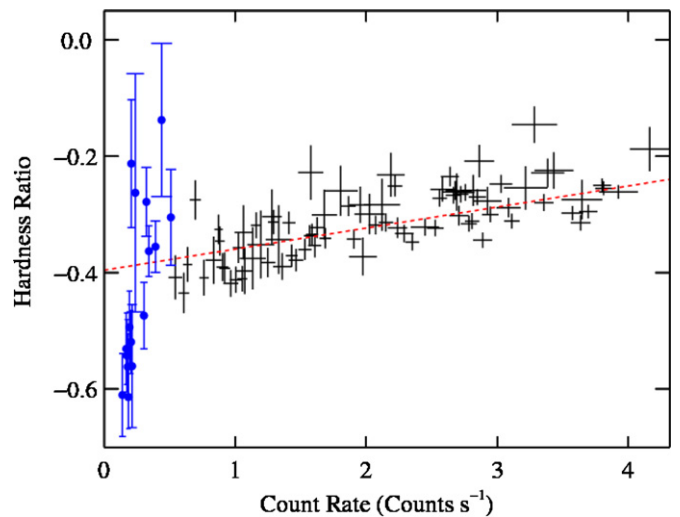


Figure 6. Hardness ratio as defined in Figure 5 vs. the full energy band of 0.5–10 keV of the *Suzaku* light curve. The red dashed line indicates the best linear fit to the points outside the eclipse. The blue points indicate the data collected during eclipse.

(A color version of this figure is available in the online journal.)

the count rate in the full energy band of 0.5–10 keV to search for a correlation between the hardness ratio and source intensity (see Figure 6). Throughout the paper, we use the weighted Pearson correlation coefficient, r (e.g., Bevington & Robinson 2003). We only take the data observed out of eclipse into account since the phenomenology is different from the data observed during eclipse (see Table 3). Out of eclipse, we found a positive correlation between the hardness ratio and source intensity ($r = 0.69$, $p \lesssim 10^{-6}$), which will be interpreted in Section 4.4.

$$\text{HR} = (C_{\text{hard}} - C_{\text{soft}})/(C_{\text{hard}} + C_{\text{soft}}). \quad (4)$$

3.3.2. PCA

To present an overview of the *RXTE* observations, we calculated the average, background-subtracted count rate of 4U 1210-64 during each spacecraft orbit and plotted this against time in Figure 7. We divided the PCA light curves into three energy bands defined between energies of 2.5–6 keV, 6–10 keV, and 10–20 keV, which are characterized by count rates C_1 , C_2 , and C_3 , respectively. Using the definition in Equation (4), we produced hardness ratios binned to a resolution of ~ 0.2 days (see Figure 7, middle and bottom). To search for correlations between the hardness ratios in each energy band, we produced a color–color diagram (see Figure 8) between the two hardness ratios to examine the correlation between them. A strong correlation was found in the color–color diagram ($r = 0.79$, $p \lesssim 10^{-6}$).

We performed a Fourier transform of all background-subtracted *RXTE* PCA Standard2 mode data together, up to a frequency of 100 cycles per day (Scargle 1982). The power spectrum is dominated by low frequency (see Figure 9), “red” noise, and the orbital period was not detected in this data set. This is likely because of a patchy orbital phase coverage.

Note that Scargle’s method is strictly correct only in judging the FAP of the highest peak mixed in with otherwise frequency-independent, “white,” noise (Scargle 1982). This is clearly not the case here. To improve our search for a spin period, we analyzed the relationship between power and frequency in log–log space to estimate and remove the amount of low-frequency red noise present in the power spectrum (Vaughan 2005).

Table 3
X-Ray Spectral Parameters for 4U 1210-64

Model Parameter	Cutoff Power Law Out-of-Eclipse	Cutoff Power Law Eclipse
χ^2_v (dof)	1.08 (2553)	0.81 (382)
Cutoff energy (keV)	5.5 ± 0.1	...
Folding energy (keV)	12 ± 1	...
Phabs N_H ($\times 10^{22}$ atoms cm^{-2})	0.70 ± 0.01	0.94 ± 0.08
Pcfabs N_H ($\times 10^{22}$ atoms cm^{-2})	$6.7^{+0.3}_{-0.4}$	11^{+2}_{-1}
Covering fraction	0.36 ± 0.03	$0.80^{+0.04}_{-0.05}$
Γ	$1.80^{+0.04}_{-0.05}$	2.9 ± 0.2
Normalization ($\times 10^{-2}$)	2.9 ± 0.2	$1.8^{+0.7}_{-0.5}$
S xv energy (keV)	2.62 ± 0.02	2.58 ± 0.05
S xv width (σ_{Sxv})	0.1^b	0.1^b
Normalization ($\times 10^{-3}$ photons $\text{cm}^{-2} \text{ s}^{-1}$)	0.11 ± 0.02	$0.11^{+0.06}_{-0.05}$
S xv EQW (eV)	20 ± 3	51^{+26}_{-22}
S xv Flux ($\times 10^{-13}$ erg $\text{cm}^{-2} \text{ s}^{-1}$)	0.54 ± 0.09	0.4 ± 0.2
Fe i energy (keV)	6.39 ± 0.01	6.4^a
Fe i width ($\sigma_{\text{Fe i}}$)	0.1^b	0.1^b
Normalization ($\times 10^{-3}$ photons $\text{cm}^{-2} \text{ s}^{-1}$)	0.093 ± 0.007	0.009^c
Fe i EQW (eV)	77^{+7}_{-5}	122^c
Fe i Flux ($\times 10^{-13}$ erg $\text{cm}^{-2} \text{ s}^{-1}$)	1.02 ± 0.08	0.7^c
Fe xxv energy (keV)	6.684 ± 0.008	6.68 ± 0.04
Fe xxv width ($\sigma_{\text{Fe xxv}}$)	0.1^b	0.1^b
Normalization ($\times 10^{-3}$ photons $\text{cm}^{-2} \text{ s}^{-1}$)	0.185 ± 0.008	0.043 ± 0.009
Fe xxv EQW (eV)	144 ± 7	392^{+160}_{-70}
Fe xxv flux ($\times 10^{-13}$ erg $\text{cm}^{-2} \text{ s}^{-1}$)	1.25 ± 0.06	1.5 ± 0.3
Fe xxvi energy (keV)	$6.970^{+0.007}_{-0.005}$	6.98 ± 0.05
Fe xxvi width ($\sigma_{\text{Fe xxvi}}$)	0.1^b	0.1^b
Normalization ($\times 10^{-3}$ photons $\text{cm}^{-2} \text{ s}^{-1}$)	$0.219^{+0.008}_{-0.009}$	0.035 ± 0.009
Fe xxvi EQW (eV)	199^{+9}_{-8}	319^{+160}_{-74}
Fe xxvi flux ($\times 10^{-13}$ erg $\text{cm}^{-2} \text{ s}^{-1}$)	1.16 ± 0.05	1.5 ± 0.4
Absorbed flux ($\times 10^{-10}$ erg $\text{cm}^{-2} \text{ s}^{-1}$)	1.024 ± 0.003	0.108 ± 0.004
Unabsorbed flux ($\times 10^{-10}$ erg $\text{cm}^{-2} \text{ s}^{-1}$)	$1.73^{+0.06}_{-0.05}$	0.16 ± 0.01

Notes.

^a The energy is frozen because we can only obtain an upper limit.

^b The natural width was frozen to 0.1 keV, the resolution of the XIS instruments.

^c The upper limit for the parameters (90% confidence interval) associated with the Fe i line is reported during eclipse.

A quadratic fit was found to give a reasonable approximation to the continuum noise level. We subtracted the quadratic fit from the logarithm of the power spectrum along with a constant value of 0.25068 to account for the bias due to the χ^2 distribution of the power spectrum (Vaughan 2005). The only statistically significant feature in the power spectrum is an artifact caused by a group of peaks around 15 cycles per day near the spacecraft orbital period (see Figure 9).

We created light curves binned to 10 ms for each GoodXenon event mode file, covering no more than a single spacecraft orbit. The estimated low-frequency red noise was removed using the procedures in Vaughan (2005), similar to what we describe above. A function that is quadratic for frequencies below $\sim 10^{-2}$ Hz and constant above this was found to give a reasonable approximation to the continuum noise level found in the log-log plot between power and frequency. The highest peak in the resulting power spectra (see Figure 10) was often found at the lowest frequency (< 0.01 mHz), presumably resulting from both source and background variability on > 100 s timescales. In five cases, additional higher frequency (> 10 Hz), apparently significant (FAP less than 0.1%) peaks were also found. However, these turned out to be related to the low-frequency peak:

the removal of the low-frequency sinusoid also removed these peaks. We conclude that these were artifacts, created by some (unknown) combination of the sampling pattern, the precise characteristics of the low-frequency variability, and possibly also the numerical limitations of the particular implementation of Scargle's algorithm that we used (Scargle 1982). Other than these, the strongest high-frequency peaks had FAP between 1% and 0.1% (note that the number of trials for each Fourier transform is taken into account, but not the fact that we analyzed 84 independent light curves), and none of these candidate frequencies repeated in multiple observations. We conclude that we did not detect the spin period of the compact object in 4U 1210-64. Scaling from the amplitudes of the highest peaks, we estimate that a sinusoidal modulation with an amplitude of 8% of the mean flux would have been detectable at 99.9% significance.

3.4. Spectral Analysis

The X-ray spectral data from the *Suzaku* and PCA observations of 4U 1210-64 were analyzed using the package XSPEC v12.8.0. We made use of the XSPEC convolution model *cflux* to calculate the fluxes and associated errors of 4U 1210-64.

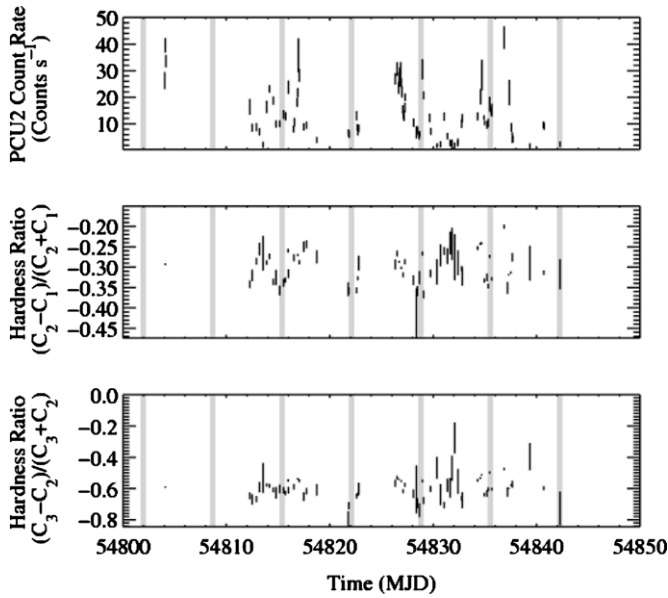


Figure 7. Long-term light curve of 4U1210-64 during the *RXTE* PCA campaign (top). We calculated the average and standard deviation of the PCU2 count rate for each spacecraft orbit. Also indicated (shaded regions) are the eclipse intervals due to the companion. Hardness ratios of the PCA light curves (middle and bottom), using bin sizes of 0.2 d., where the energy bands for C_1 , C_2 , and C_3 are 2.5–6 keV, 6–10 keV, and 10–20 keV, respectively.

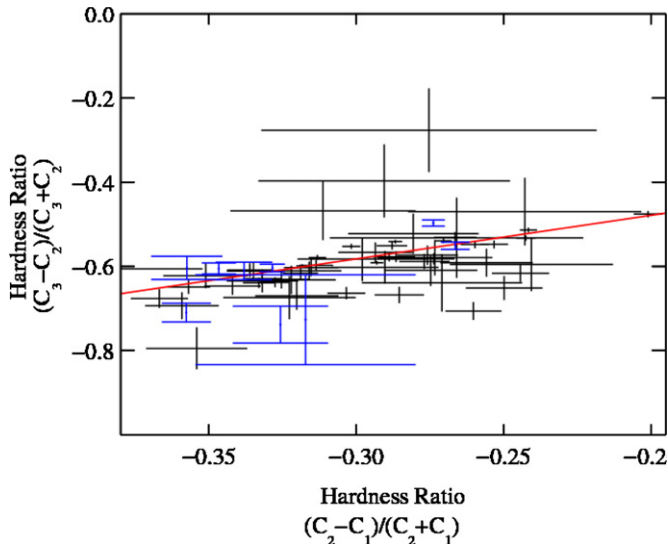


Figure 8. PCA color-color diagram comparing soft color vs. hard color as defined in Figure 7. The red line indicates the best linear fit to the points outside the eclipse. The blue points indicate the data collected during eclipse.

(A color version of this figure is available in the online journal.)

3.4.1. *Suzaku* Spectral Analysis

To fit the *Suzaku* spectra, we used several models: a power law, thermal bremsstrahlung, a power law modified with a high-energy cutoff (see Figure 11), and emission due to collisionally ionized diffuse gas (APEC in XSPEC; Foster et al. 2012). All models were modified by a partially covering absorber in addition to an absorber that fully covers the source using the Balucinska-Church & McCammon (1992) cross sections and Wilms et al. (2000) abundances.

The model that provides a good fit to the data is a power law modified by a high-energy cutoff (reported in Table 3). We find that the neutral hydrogen column densities for fully

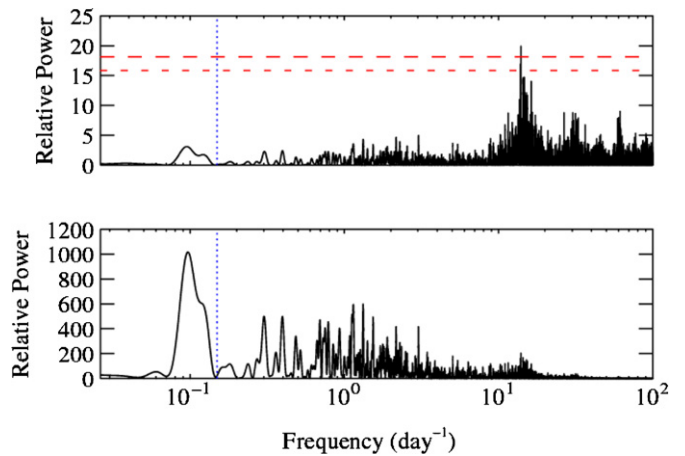


Figure 9. Scargle's power spectrum of the PCA data up to a frequency of 100 cycles per day with the estimated continuum noise component removed (top). The uncorrected power spectrum (bottom) is dominated by strong low-frequency variability. The orbital period (see Sections 3.1.1 and 3.1.2) is indicated by the blue dashed line. The red short-dashed line is the power corresponding to 1% FAP, and the red long-dashed line is the power corresponding to 0.1% FAP.

(A color version of this figure is available in the online journal.)

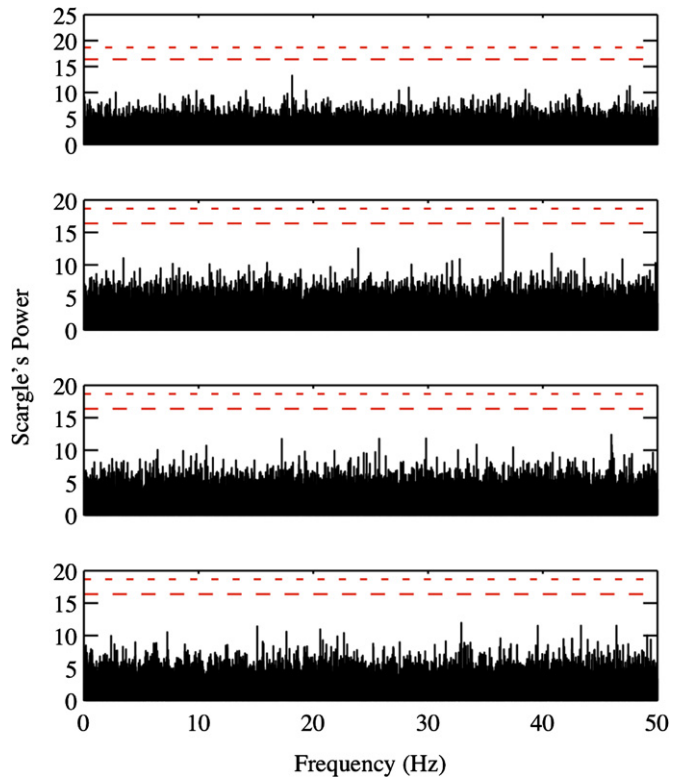


Figure 10. Typical PCA power spectra for ObsID 99009-01-01-17 (top), ObsID 99009-01-01-22 (second from top), ObsID 99009-01-23-00 (third panel), and ObsID 99009-01-03-02 (bottom). The frequency range is from 5.73×10^{-4} –50 Hz. The long-dashed line is the power corresponding to 1% FAP, and the short-dashed line is the power corresponding to 0.1% FAP. The highest peak in the ObsID 99009-01-01-22 power spectrum is found to be between the 99% and 99.9% confidence intervals (second from top).

(A color version of this figure is available in the online journal.)

covered and partially covering absorption are $N_H = 0.70 \pm 0.01 \times 10^{22}$ and $N_H = 6.7^{+0.3}_{-0.4} \times 10^{22}$ atoms cm^{-2} , respectively, with a partial covering fraction of 0.36 ± 0.03 . The measured values of the fully covered absorber are comparable to the Galactic H I values reported by the Leiden/Argentine/Bonn

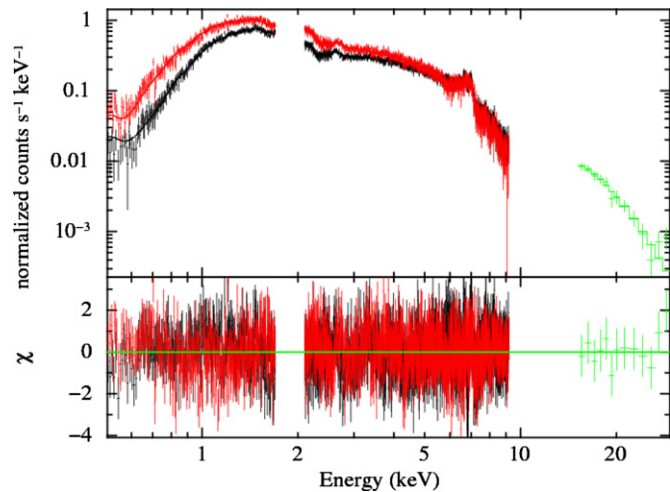


Figure 11. One of the best-fit models for 4U 1210-64, where XIS0+3, XIS1, and HXD/PIN are indicated by the black, red, and green data/models, respectively. This consists of a continuum comprised of a power law with a high-energy cutoff and four emission lines composed of S xvi K α , Fe K α , Fe xxv K α , and Fe xxvi K α . The continuum is absorbed by partial covering absorption and fully covering absorption.

(A color version of this figure is available in the online journal.)

survey (Kalberla et al. 2005) and in the review by Dickey & Lockman (1990), which are 8.16×10^{21} and 9.37×10^{21} atoms cm $^{-2}$, respectively. Therefore, we assume that the fully covered absorber is interstellar in origin unless otherwise noted (see Section 4.4 for treatment in eclipse). A good fit does not require an additional blackbody component, even though such a soft excess was seen in the *INTEGRAL* data by Masetti et al. (2010). Furthermore, we do not detect any cyclotron lines in the *Suzaku* spectra.

Emission features in the Fe K α region were detected at 6.4 keV, 6.7 keV, and 6.97 keV; which were modeled using a Gaussian centered on the peak of the lines (see Figure 12). We interpret these features as Fe K α , Fe xxv K α , and Fe xxvi K α , respectively (see Figure 12). In addition, an emission line was observed at 2.6 keV, which we interpret as S xvi K α (see Figure 12).

We investigated temporal dependence of the spectral parameters, comparing the parameters during eclipse to those out of eclipse. The out-of-eclipse region was subdivided into several 10 ks intervals to further investigate the temporal variability of the spectral parameters. Since 4U 1210-64 is not easily detectable in the HXD-PIN for much of the observation, we only considered the XIS spectra for the analysis of time dependent changes in spectral parameters. A good fit to the spectra does not require a high-energy cutoff, although it is needed for the time-averaged out-of-eclipse spectrum for which we analyzed the well-exposed HXD-PIN spectrum along with the XIS data. We choose to model the spectra using a power law with a high-energy cutoff frozen at the values of the time-averaged spectra (see Table 4). The Fe I line was not detected during eclipse (see Table 3). We therefore derived an upper limit for the strength of the line.

In order to place constraints on the origin of the Fe K α lines, we compared the flux of the Fe K α lines with the unabsorbed continuum flux in the 7.1–9.0 keV band (see Figure 13). The flux of the Fe I line is found to decrease by a factor of ~ 15 during eclipse (see Table 4). Additionally, we found that the flux of Fe xxv and Fe xxvi decreases by a factor of approximately

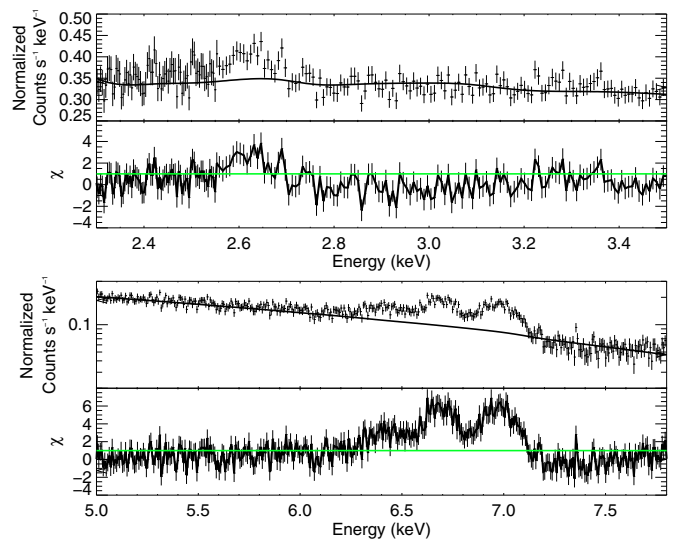


Figure 12. XIS0+3 spectrum of 4U 1210-64 in the 2.3–3.5 keV (top) and 5.0–7.8 keV bands (third panel) to illustrate the S xvi and Fe K α emission lines along with the best-fit model. The normalization of the lines was set to zero in the model. Residuals are plotted in the second from top and bottom panels.

(A color version of this figure is available in the online journal.)

three during the eclipse phase (see Table 4). Within measurement errors, the flux of the Fe K α lines observed out of eclipse was found to follow the flux of the continuum. The correlation coefficients, r , are as follows: $r = 0.82$, $r = 0.81$, and $r = 0.87$ for the Fe I, Fe xxv, and Fe xxvi lines, respectively. Using a logarithmic parameter space, we measured the slope of the Fe K α line flux observed out of eclipse versus continuum flux— $m = 1.0 \pm 0.1$, $m = 0.6 \pm 0.1$ and $m = 0.7 \pm 0.1$ for the Fe I, Fe xxv, and Fe xxvi lines, respectively.

To constrain the state of the plasma, we calculated the flux ratio between the Fe xxv and Fe xxvi emission features. We defined the flux ratio as the flux of the Fe xxv line divided by the flux of the Fe xxvi line. No change was found in the flux ratio between the Fe xxv and Fe xxvi emission features and the continuum flux in the 7.1–9.0 keV band (see Table 4).

In contrast to the Fe K α lines, the S xvi K α line was not consistently detected throughout the duration of the *Suzaku* observation (see Table 4). During the time intervals specified in Table 4, we calculated an upper limit of the EQW and flux of the S xvi line at the 90% confidence interval. We also searched for correlations between the continuum spectral parameters (the power law with the high-energy cutoff modified with fully covered and partial covering absorption) with respect to the 7.1–9.0 keV continuum flux (see Table 4). We found no clear correlation between the parameter values and flux.

In addition, we found that a bremsstrahlung model with a temperature of 7.2 ± 0.2 keV also fits the *Suzaku* data reasonably well. However, this model is found to provide unsatisfactory fits to the PCA spectra where χ^2_ν was found to exceed two (see Section 3.4.2). Therefore, the power law with the high-energy cutoff model is the preferred description of 4U 1210-64.

3.4.2. PCA Spectral Analysis

We analyzed the PCA spectral data of 4U 1210-64 from MJD 54804–54842, using the models described in Section 3.4.1. The best-fit model is a power law with a high-energy cutoff (see Figure 14, top and middle). Due to the lack of low-energy response (see Section 2.1.2), the absorption that is observed

Table 4
Spectral Parameters of 4U 1210-64 of the *Suzaku* Observation Using a Power-law Continuum with a High-energy Cutoff^a

Time ^b (ks)	Phabs N_H (10^{22} cm^{-2})	Pcfabs N_H (10^{22} cm^{-2})	Cvr	Γ	EQW S xvi (eV)	EQW Fe i (eV)	EQW Fe xxv (eV)	EQW Fe xxvi (eV)	Flux Ratio ^c	F_{unabs} ($10^{-10} \text{ erg cm}^{-2} \text{ s}^{-1}$)	χ^2_v (dof)
0–22.5	0.93 ± 0.08	11^{+2}_{-1}	$0.80^{+0.04}_{-0.05}$	2.9 ± 0.2	51^{+26}_{-22}	70^d	420^{+162}_{-76}	364^{+156}_{-83}	1.0 ± 0.3	0.53 ± 0.03	0.82(382)
30–40	0.76 ± 0.06	8 ± 2	$0.49^{+0.07}_{-0.08}$	1.9 ± 0.1	48^e	118^{+50}_{-36}	231^{+53}_{-40}	147^{+47}_{-37}	$1.3^{+0.5}_{-0.4}$	1.0 ± 0.1	0.92(499)
40–50	$0.71^{+0.04}_{-0.05}$	4 ± 1	0.33 ± 0.05	$1.69^{+0.07}_{-0.06}$	16^e	55^{+19}_{-20}	100^{+28}_{-25}	174^{+39}_{-32}	1.2 ± 0.3	2.1 ± 0.1	0.96(1146)
50–60	0.69 ± 0.03	5.7 ± 0.9	0.38 ± 0.04	1.76 ± 0.05	24^{+7}_{-8}	67^{+14}_{-13}	100^{+18}_{-15}	171^{+21}_{-19}	1.0 ± 0.2	2.5 ± 0.1	0.97(2030)
60–70	0.75 ± 0.02	6.3 ± 0.7	0.43 ± 0.04	1.94 ± 0.05	18 ± 8	65^{+16}_{-13}	121^{+19}_{-16}	193^{+23}_{-19}	1.0 ± 0.2	$3.0^{+0.2}_{-0.1}$	0.92(2094)
70–80	0.76 ± 0.03	6.6 ± 0.9	0.41 ± 0.04	1.97 ± 0.06	18 ± 9	50^{+17}_{-15}	205^{+26}_{-21}	206^{+27}_{-25}	1.2 ± 0.2	2.1 ± 0.1	0.97(1572)
80–90	$0.68^{+0.04}_{-0.05}$	5 ± 2	0.32 ± 0.07	1.84 ± 0.09	23^{+12}_{-13}	59^{+26}_{-22}	158^{+33}_{-26}	263^{+47}_{-39}	1.2 ± 0.3	1.3 ± 0.1	0.96(1103)
90–100	0.72^f	6 ± 1	$0.35^{+0.08}_{-0.09}$	$1.95^{+0.08}_{-0.09}$	42^{+16}_{-15}	129^{+31}_{-29}	203^{+37}_{-31}	264^{+46}_{-41}	$1.0^{+0.3}_{-0.2}$	$0.82^{+0.07}_{-0.06}$	0.94(809)
100–110	0.67 ± 0.05	12 ± 3	0.3 ± 0.1	1.6 ± 0.1	26^{+17}_{-18}	108^{+33}_{-27}	207^{+45}_{-31}	174^{+45}_{-31}	$1.1^{+0.4}_{-0.3}$	1.2 ± 0.1	0.91(631)
110–120	0.70 ± 0.04	9 ± 1	$0.42^{+0.06}_{-0.07}$	1.69 ± 0.08	15^{+12}_{-13}	88^{+23}_{-20}	110^{+25}_{-20}	168^{+32}_{-27}	1.2 ± 0.3	2.8 ± 0.2	0.96(1022)
120–130	$0.66^{+0.04}_{-0.05}$	5 ± 2	0.27 ± 0.07	1.73 ± 0.08	20^{+11}_{-12}	31^{+21}_{-20}	155^{+31}_{-25}	215^{+38}_{-30}	1.0 ± 0.3	$2.1^{+0.2}_{-0.1}$	0.96(1021)
130–140	0.70 ± 0.03	9 ± 1	0.37 ± 0.07	$1.86^{+0.09}_{-0.08}$	38^{+13}_{-12}	26^{+21}_{-20}	247^{+37}_{-28}	206^{+34}_{-25}	$1.0^{+0.4}_{-0.2}$	1.4 ± 0.1	1.07(1036)
140–150	0.66 ± 0.03	7 ± 1	0.30 ± 0.06	1.66 ± 0.06	17^e	101^{+18}_{-17}	126^{+21}_{-16}	190^{+24}_{-23}	1.1 ± 0.2	1.9 ± 0.1	0.95(1616)
150–160	0.72 ± 0.03	7 ± 1	$0.40^{+0.06}_{-0.07}$	1.89 ± 0.08	16 ± 12	78^{+23}_{-20}	198^{+34}_{-25}	231^{+33}_{-28}	$1.1^{+0.3}_{-0.2}$	1.4 ± 0.1	0.98(1108)
160–170	0.63^f	16^{+13}_{-5}	$0.23^{+0.08}_{-0.09}$	$1.64^{+0.08}_{-0.07}$	61 ± 16	161^{+34}_{-30}	164^{+44}_{-27}	242^{+44}_{-36}	1.1 ± 0.3	$0.70^{+0.05}_{-0.04}$	0.99(786)

Notes. The best-fit parameters for the eclipse and out of eclipse, which is subdivided into 10 ks time intervals.

^a The cutoff and folding energies of the high-energy cutoff are frozen to the best-fit values of the out-of-eclipse spectrum: 5.5 keV and 12.0 keV, respectively.

^b Time is relative to the start of the *Suzaku* observation, MJD 55553.16.

^c The ratio of the strengths of the Fe xxv line with respect to the Fe xxvi line.

^d The upper limit for the EQW of the Fe i line at the 90% confidence interval is reported during eclipse.

^e The upper limit for the EQW of the S xvi line at the 90% confidence interval is reported at the time intervals of 30–40 ks, 40–50 ks, and 140–150 ks.

^f The fully covered absorber is frozen to the value that was extracted using the power-law model.

in the *Suzaku* spectra cannot be accurately measured using the PCA (see Section 3.4.1). Therefore, we froze N_H to the out-of-eclipse value determined with *Suzaku*.

The power-law index, Γ , and cutoff energies found with the PCA are consistent with those determined with the *Suzaku* analysis. However, we note that the folding energy obtained with the PCA differs somewhat from that obtained with *Suzaku*. We also note that the folding energy was found to be variable among different time segments of PCA data.

Due to the ~ 10 times lower spectral resolution of the PCA compared with *Suzaku* (see Sections 2.1.2 and 2.4.1, respectively), we detected only a broad emission feature between energies of 6.4–6.7 keV in the Fe K α region, which was modeled using a single Gaussian (see Figure 14, bottom). Furthermore, the S xvi K α feature was not detected in the PCA spectra, which is expected due to the low sensitivity of the PCA at 2.62 keV.

The temporal dependence of the spectral parameters was investigated (see Table 5). We searched for correlations between the continuum spectral parameters (the folding energy, the high-energy cutoff, and the power-law index) with respect to the 2.5–20 keV continuum flux (see Figure 15). While no clear correlation between the folding energy and flux was found, the high-energy cutoff and power-law index are anti-correlated in respect to the continuum flux. The correlation coefficients (r) are: -0.69 and -0.81 for the high-energy cutoff and power-law index, respectively.

4. DISCUSSION

In our analysis of 4U 1210-64, we found the presence of an eclipse, long- and short-term variability, and an Fe K α emission complex. Below, we discuss constraints on the mass donor based on the eclipse half-angle, the nature of the compact object, the

variability found in the system, and the mechanism responsible for the Fe K α emission seen in 4U 1210-64.

The source emission does not reach 0 counts s^{-1} in the folded light curves (see Section 3.2). Residual emission was also found in the *Suzaku* and PCA observations (see Tables 3–5). While residual emission has been attributed to a dust-scattering in some other HMXBs (Cen X-3; Vela X-1; OAO 1657-415, Day & Tennant 1991; Woo et al. 1994; Audley et al. 2006), the residual emission found in 4U 1210-64 is seen at much higher levels compared to the out-of-eclipse emission, and is found in both MAXI (2–20 keV) and PCA (2.5–20 keV). A dust-scattering halo is predominantly a soft X-ray phenomenon: given the interstellar N_H (see Table 3), we infer perhaps 10%–20% of the out-of-eclipse flux at 1 keV may be in a dust-scattering halo (Predehl & Schmitt 1995), but a much smaller fraction in the MAXI and the PCA band. Since we detect Fe xxv and Fe xxvi lines in eclipse, indicating the presence of an extended region of ionized gas, we believe it is plausible that Compton scattering and reprocessing can account for the residual flux in eclipse (Watanabe et al. 2006).

4.1. Constraints on the Mass-Donor

Our analysis of the ASM, MAXI, and BAT folded light curves reveals the presence of a sharp dip, which is suggestive of an eclipse (see Section 3.2).

4.1.1. Eclipse Half-angle Constraints

X-ray binaries that are eclipsing have an eclipse duration (see Section 3.2) that is dependent on the radius of the mass donor, inclination angle of the system, and the orbital separation of the components. Using the observed orbital period and Kepler's third law, the phenomenon can be written in terms of the sum

Table 5
Spectral Parameters of 4U 1210-64 of the PCA Observations Using a Power-law Continuum with a High-energy Cutoff

Time (MJD)	Phabs N_{H} (10^{22} cm^{-2})	Pcfabs N_{H} (10^{22} cm^{-2})	Cvr	High-energy Cutoff (keV)	Folding Energy (keV)	Power-law Γ	Power-law Normalization (10^{-2})	Fe K α Energy (keV)	EQW Fe K α (eV)	F_{unabs} ($10^{-10} \text{ erg cm}^{-2} \text{ s}^{-1}$)	χ^2_{ν} (dof)
54804	0.70 ^a	6.74 ^a	0.36 ^a	6.0 \pm 0.1	5.6 \pm 0.1	1.50 \pm 0.03	7.8 \pm 0.3	6.66 ^{+0.01} _{-0.02}	228 ⁺²⁶ ₋₁₈	7.4 \pm 0.2	0.82(35)
54812	0.70 ^a	6.74 ^a	0.36 ^a	7.4 \pm 0.2	5.5 \pm 0.4	1.96 \pm 0.04	4.6 \pm 0.3	6.65 ^{+0.01} _{-0.07}	414 ⁺⁵² ₋₃₉	1.71 \pm 0.04	0.49(35)
54813	0.70 ^a	6.74 ^a	0.36 ^a	6.6 \pm 0.3	7.0 ^{+0.5} _{-0.4}	1.70 \pm 0.05	3.2 \pm 0.2	6.59 ^{+0.08} _{-0.02}	306 ⁺³⁰ ₋₃₆	2.01 \pm 0.06	0.71(35)
54814	0.70 ^a	6.74 ^a	0.36 ^a	6.5 \pm 0.2	5.9 \pm 0.3	1.70 \pm 0.04	4.6 ^{+0.3} _{-0.2}	6.66 \pm 0.09	159 ⁺²⁷ ₋₃₂	2.86 \pm 0.08	0.35(35)
54815	0.70 ^a	6.74 ^a	0.36 ^a	6.3 \pm 0.2	6.8 ^{+0.2} _{-0.3}	1.70 \pm 0.03	5.0 \pm 0.2	6.662 ^{+0.004} _{-0.085}	250 ⁺³² ₋₂₃	3.08 ^{+0.07} _{-0.06}	0.74(35)
54816	0.70 ^a	6.74 ^a	0.36 ^a	5.9 \pm 0.2	6.9 ^{+0.3} _{-0.2}	1.43 \pm 0.03	4.2 \pm 0.2	6.61 ^{+0.03} _{-0.04}	297 ⁺³⁷ ₋₃₆	4.6 \pm 0.1	1.00(34)
54817	0.70 ^a	6.74 ^a	0.36 ^a	6.1 \pm 0.2	6.2 ^{+0.4} _{-0.3}	1.51 \pm 0.05	3.5 \pm 0.2	6.56 ^{+0.04} _{-0.05}	318 ⁺⁴⁷ ₋₄₆	3.3 \pm 0.1	0.51(34)
54818	0.70 ^a	6.74 ^a	0.36 ^a	7.6 ^{+0.7} _{-1.0}	10 ⁺³ ₋₂	2.01 ^{+0.08} _{-0.11}	1.7 ^{+0.2} _{-0.3}	6.486 ^{+0.002} _{-0.085}	909 ⁺¹⁷⁵ ₋₁₃₅	0.60 ^{+0.04} _{-0.02}	0.55(35)
54821	0.70 ^a	6.74 ^a	0.36 ^a	7.6 ^{+0.2} _{-0.3}	4.7 ^{+0.6} _{-0.5}	2.20 \pm 0.05	4.3 \pm 0.3	6.669 ^{+0.089} _{-0.001}	502 ⁺⁵¹ ₋₆₂	1.00 \pm 0.02	0.70(35)
54822 ^b	0.94	10.73	0.80	8.1 \pm 0.2	8.7 ^{+0.8} _{-0.7}	2.56 ^{+0.02} _{-0.03}	13.5 \pm 0.5	6.67 \pm 0.01	440 ⁺²⁶ ₋₃₉	1.63 \pm 0.01	1.17(35)
54826	0.70 ^a	6.74 ^a	0.36 ^a	6.5 \pm 0.1	7.4 \pm 0.2	1.63 \pm 0.02	7.1 ^{+0.3} _{-0.2}	6.63 ^{+0.04} _{-0.05}	160 ⁺¹⁶ ₋₁₄	5.01 \pm 0.08	1.00(35)
54827	0.70 ^a	6.74 ^a	0.36 ^a	6.7 \pm 0.2	6.5 ^{+0.4} _{-0.3}	1.79 \pm 0.04	5.4 \pm 0.3	6.67 \pm 0.06	306 ⁺²³ ₋₃₄	2.79 ^{+0.07} _{-0.06}	0.83(35)
54828	0.70 ^a	6.74 ^a	0.36 ^a	7.3 \pm 0.2	6.9 \pm 0.4	1.86 \pm 0.04	5.3 \pm 0.3	6.63 ^{+0.02} _{-0.07}	305 ⁺³⁹ ₋₂₇	2.41 \pm 0.05	1.07(35)
54829 ^b	0.94	10.73	0.80	8.5 \pm 0.4	11 \pm 2	2.62 \pm 0.03	18.1 \pm 0.9	6.48 ^{+0.01} _{-0.08}	485 ⁺⁵⁶ ₋₄₅	1.98 \pm 0.02	1.69(35)
54830	0.70 ^a	6.74 ^a	0.36 ^a	6.6 ^c	6.6 ^c	1.82 \pm 0.08	0.7 \pm 0.1	6.51 ^{+0.06} _{-0.03}	696 \pm 105	0.36 \pm 0.01	0.87(37)
54831	0.70 ^a	6.74 ^a	0.36 ^a	8.1 \pm 0.5	10 ⁺³ ₋₂	2.12 \pm 0.06	3.0 ^{+0.2} _{-0.3}	6.59 \pm 0.03	1061 ⁺¹⁵⁹ ₋₁₃₁	0.85 \pm 0.02	0.81(34)
54832	0.70 ^a	6.74 ^a	0.36 ^a	7.0 \pm 0.3	7.1 ^{+0.7} _{-0.6}	1.96 \pm 0.05	2.9 \pm 0.2	6.54 ^{+0.04} _{-0.05}	568 ⁺⁵⁶ ₋₃₉	1.07 \pm 0.02	0.77(35)
54834	0.70 ^a	6.74 ^a	0.36 ^a	6.6 \pm 0.2	7.5 \pm 0.2	1.55 \pm 0.03	4.1 \pm 0.2	6.49 \pm 0.04	267 ⁺¹⁵ ₋₂₀	3.43 \pm 0.07	1.07(35)
54835	0.70 ^a	6.74 ^a	0.36 ^a	6.7 ^{+0.1} _{-0.2}	7.2 ^{+0.3} _{-0.2}	1.75 \pm 0.03	4.5 \pm 0.2	6.66 \pm 0.09	148 ⁺¹⁹ ₋₁₆	2.53 \pm 0.06	0.84(35)
54836	0.70 ^a	6.74 ^a	0.36 ^a	7.8 ^{+0.2} _{-0.3}	9.8 ^{+0.5} _{-0.4}	1.58 \pm 0.03	9.4 ^{+0.4} _{-0.3}	6.488 ^{+0.086} _{-0.002}	312 ⁺³⁶ ₋₄₁	7.5 \pm 0.2	0.79(35)
54837	0.70 ^a	6.74 ^a	0.36 ^a	6.4 \pm 0.1	6.3 \pm 0.1	1.73 \pm 0.02	5.6 \pm 0.2	6.68 ^{+0.07} _{-0.01}	236 ⁺¹⁴ ₋₁₇	3.26 \pm 0.05	0.95(35)
54839	0.70 ^a	6.74 ^a	0.36 ^a	6.6 ^c	6.6 ^c	1.7 \pm 0.2	0.41 ^{+0.12} _{-0.09}	6.4 \pm 0.1	570 ⁺²⁰² ₋₁₈₂	0.27 \pm 0.02	0.94(37)
54840	0.70 ^a	6.74 ^a	0.36 ^a	6.6 ^{+0.6} _{-0.3}	7.8 \pm 0.6	1.90 ^{+0.03} _{-0.04}	3.8 ^{+0.4} _{-0.2}	6.73 ^{+0.04} _{-0.13}	362 ⁺⁴⁸ ₋₄₇	1.59 \pm 0.05	0.55(35)
54842 ^b	0.94	10.73	0.80	7.9 ^d	8.0 ^d	2.5 \pm 0.1	3.3 ^{+0.8} _{-0.6}	6.9 \pm 0.2	529 ⁺²¹⁷ ₋₂₁₁	0.50 \pm 0.03	0.55(37)

Notes. The best-fit parameters for the PCA spectra.

^a Out of eclipse, the fully covered absorber and partially covered absorber are frozen to the best-fit values of the *Suzaku* out-of-eclipse spectrum (see Table 3).

^b Time intervals when 4U 1210-64 is in eclipse. N_{H} is frozen to the best-fit values of the *Suzaku* eclipse spectrum (see Table 3).

^c The cutoff energy and folding energy parameters at these time intervals are frozen to the weighted average of the out-of-eclipse spectra.

^d The cutoff energy and folding energy parameters at these time intervals are frozen to the weighted average of the eclipse spectra.

of the donor star and compact object masses, which stipulates that the eclipse half-angle, Θ_e , can now be expressed in terms of the radius, inclination, and masses of the components. In one set of calculations, we assume a $1.4 M_{\odot}$ compact object, which may be appropriate for an accreting neutron star. The region allowed by the measured eclipse half-angle for 4U 1210-64 in the mass–radius plot is shown in Figure 16 (shaded region). Its inclination is constrained between edge-on orbits (left boundary of the shaded region in Figure 16) and close to face-on orbits (the right boundary of the shaded region in Figure 16). We can attach additional constraints assuming that the mass donor underfills the Roche-lobe radius, which is dependent on the mass ratio of the system and the orbital separation (see Figure 16, bottom boundary). To calculate the eclipse half-angle and the Roche lobe radius, we used Equation (E.4) in Chakrabarty (1996) and Equation (2) in Eggleton (1983), respectively. We additionally calculated the minimum inclination angle of the system, i_{min} , which is consistent with the measured eclipse half-angle (see Table 6 and Figure 17). An intriguing result is that the duration of the observed eclipse is inconsistent with the proposed B5 V spectral type (see Figure 17). A B5 V has a mass of $5.9 M_{\odot}$ according to Carroll & Ostlie (2006) and Allen (2000). For a donor star of $5.9 M_{\odot}$ to satisfy the eclipse half-angle constraint, we calculated that the radius must exceed $5.37 R_{\odot}$. This is

clearly larger than the radii reported in Carroll & Ostlie (2006) and Allen (2000), which is $4.1 R_{\odot}$ and $3.9 R_{\odot}$, respectively (see Table 6). Therefore, the radius of a B5 V is too small to satisfy our observed eclipse duration (see Figure 16).

The eclipse half-angle was calculated as a function of inclination angle for other B-type stars—B0 V, B5 III, B0 III, B5 I, and B0 I (see Figure 17). The eclipse half-angle was found to be consistent with a main-sequence star of spectral class B0 V only at high inclination angles (see Table 6). We also consider intermediate and late spectral types in our analysis (see Figures 16 and 17). These will be discussed in Section 4.1.3.

We also calculated the eclipse half-angle as a function of the inclination angle for these stars under the assumption of more massive compact objects. The results are presented in Figures 16 and 17 for the scenario of a $1.9 M_{\odot}$ neutron star, which is one of the highest known masses for neutron stars in XRBs (Lattimer 2012). Our results remained the same for more substantial mass donors. However, the results require slightly higher inclination angles for intermediate and late spectral types (see Figure 16).

The spectral type of the mass donor places an additional constraint on the distance of 4U 1210-64. Under the assumption that the *R*-band magnitude (m_R) and extinction in the *V* band (A_V) are magnitudes 13.9 and 3.3 for a B5 V classification (Masetti et al. 2009), the distance and average X-ray luminosity

Table 6
Physical Parameters for Candidate Mass Donors in 4U 1210–64

Spectral Type	M/M_{\odot}	R/R_{\odot}	R_L/R_{\odot} ^a	M_V	$(B - R)_0$ ^b	$E(B - R)$ ^b	i_{\min} ^c	d_{sun} ^d (kpc)	d_{gal} ^e (kpc)	L_{xavg} ($\times 10^{35} \text{ erg s}^{-1}$)
B5 V ^f	<i>5.9</i>	<i>4.1</i>	13.7	<i>−1.2</i>	−0.21	1.71	... ^g	~2.8	~7.4	~1.6
B5 V ^f	5.9	3.9	13.7	<i>−1.2</i>	−0.21	1.71	... ^g	~2.8	~7.4	~1.6
B0 V	<i>18</i>	<i>8.4</i>	23.1	<i>−4.0</i>	−0.40	1.90	84	~9.8	~9.3	~20.0
B5 III	<i>7.0</i>	<i>6.3</i>	14.9	<i>−2.2</i>	−0.21	1.71	85	~4.1	~7.3	~3.4
B0 III	<i>20</i>	<i>13</i>	24.6	<i>−5.1</i>	−0.34	1.84	75	~15	~13	~44.6
B5 I	<i>20</i>	<i>41</i>	24.6	<i>−6.2</i>	−0.10	1.60	9	~29	~26	~175
B0 I	<i>25</i>	<i>25</i>	27.2	<i>−6.4</i>	−0.36	1.86	57	~31	~28	~197
F0 III	<i>2.0</i>	<i>5.0</i>	7.7	<i>1.5</i>	0.45	1.05	82	~0.9	~7.9	~0.2
G0 III	<i>1.0</i>	<i>5.7</i> ^h	5.2 ^h	<i>1.0</i>	1.11	0.39	77	~1.3	~7.8	~0.3

Notes. The values in italics are obtained from Carroll & Ostlie (2006) and Masetti et al. (2009). The values in both italics and bold are obtained from Allen (2000) in comparison with those in Carroll & Ostlie (2006).

^a The definition for the Roche lobe, R_L , as given in Eggleton (1983), assuming M_{NS} is $1.4 M_{\odot}$.

^b The value for $(B - R)_0$ was calculated using $(B - V)_0$ and $(R - V)_0$, published in Wegner (1994). $E(B - R)$ is found by subtracting $(B - R)_0$ from the observed $B - R$ (see Section 4.1.2).

^c The minimum inclination angle of the system that is consistent with the measured eclipse half-angle.

^d The distance the object is from the Sun.

^e Galactocentric distance of 4U 1210-64.

^f Masetti et al.'s (2009) proposed spectral type and distance of the object.

^g A B5 V classification is inconsistent with the observed eclipse half-angle.

^h A G0 III classification significantly overfills the Roche lobe assuming a $1.4 M_{\odot}$ compact object.

of the source are found to be ~ 2.8 kpc and $1.79 \pm 0.02 \times 10^{35} \text{ erg s}^{-1}$, respectively (see Table 6). We calculated the extinction in the V band (A_V) using Equation (1) in Güver & Oumlzel (2009) and the measured neutral hydrogen column densities for the fully covered absorber (see Table 4). A_V was found to be 3.2 ± 0.1 for the power law with high-energy cutoff model.

The distance and average X-ray luminosity of 4U 1210-64 assuming the aforementioned spectral types is reported in Table 6 using the values for M_V and A_R obtained from Carroll & Ostlie (2006). A B0 V star places the system at an estimated distance of ~ 9.5 kpc away from the Sun, indicating that 4U 1210-64 could be located in the Carina arm (approximately 10 kpc). A supergiant classification places 4U 1210-64 at a galactocentric distance exceeding ~ 26 kpc, which is outside of the Galaxy. Therefore, the possibility of a supergiant must be excluded. Since Masetti et al.'s (2009) previous classification must also be excluded due to the observed eclipse duration, it is possible that the mass donor could be an early B-type giant or an early F-type giant (see Section 4.1.3). Main-sequence stars with the exception of very early types and very high inclination angles are also excluded.

4.1.2. Does the Proposed Mass Donor Spectral Type Agree with Masetti's Optical Spectrum?

The duration of the eclipse along with the constraint that the mass donor must underfill the Roche lobe allows for the possibility of several different spectral types (see Sections 4.1 and 4.1.3). We compared the expected optical spectra for each proposed mass donor with Masetti et al.'s (2009) optical spectrum (the top-right panel in Figure 4) to place an additional constraint on the nature of the mass donor. Since the 4000–5000 Å region is compressed in Masetti et al.'s (2009) broadband spectrum, there are possible caveats in the identification of spectral features to correctly classify the mass donor.

The features observed in Masetti et al.'s (2009) optical spectrum include absorbed Balmer series lines and the emission of neutral helium, singly ionized helium, and a blend of doubly

ionized nitrogen and carbon. The optical spectra of B-type stars are expected to show the absorption of neutral helium and H α lines (Carroll & Ostlie 2006, and references therein). Singly ionized calcium features at ~ 3900 Å become dominant in F-type stars (Carroll & Ostlie 2006, and references therein), which would be difficult to detect in Masetti et al.'s (2009) broadband spectrum. The stellar luminosity type can also in principle be determined using spectral lines, which could lead to distinguishing a B III- or B V-type. For B5 stars, the ratio of Si II to Si III as well as the Al III and Fe III lines can be used to determine luminosity type (Gray & Corbally 2009). Unfortunately, the existing optical spectra are not suitable in detecting these effects.

The observed value of the $B - R$ color of 1.5^{11} was compared with the intrinsic $(B - R)_0$ for the proposed mass donors (see Table 6). Calculating the difference between the observed $B - R$ and the intrinsic $(B - R)_0$, we found the reddening values $E(B - R)$ for each proposed spectral type for the mass donor (see Table 6). We calculated the reddening in the $B - V$ band, $E(B - V)$, using Equation (1) in Güver & Oumlzel (2009) and the measured neutral hydrogen column densities for fully covered absorber (see Table 4). We converted $E(B - V)$ to $E(B - R)$ using Table 3 in Rieke & Lebofsky (1985). We found $E(B - R)$ to be 1.82 ± 0.08 for the power law with high-energy cutoff model, where the reddening was found to be consistent with main-sequence and giant B-type stars, but was inconsistent with F-types. Since a B5 V classification does not satisfy the eclipse half-angle, the optical features might indicate that the mass donor is a B-type giant. We note the optical spectra of B-type giants would be difficult to distinguish from that of main-sequence B-type stars because of the low resolution of Masetti et al.'s (2009) broadband spectrum. F-type giants cannot be completely excluded due to systematic effects, which prevent a definite determination. For example, we assumed that the fully covered N_H is entirely interstellar in origin (see Section 3.4.1). While this is the simplest interpretation of the data, we cannot exclude the possibility that the fully covered N_H is due to a

¹¹ <http://www.iasfbo.inaf.it/~masetti/IGR/main.html>

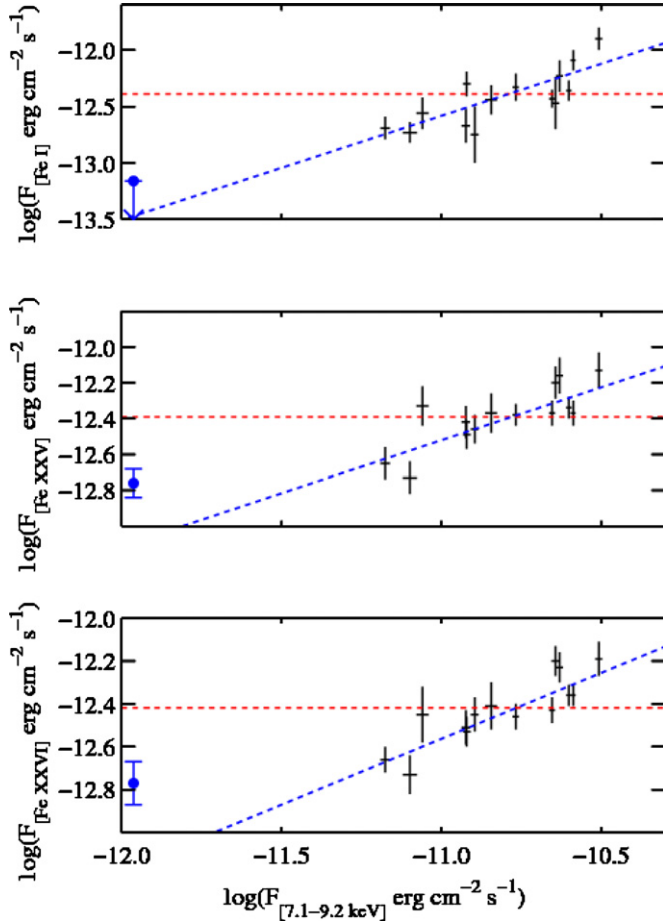


Figure 13. Flux of the Fe I (top), Fe XXV (middle), and Fe XXVI (bottom) lines vs. the unabsorbed continuum flux in the 7.1–9.0 keV band in logarithmic units. An upper limit at the 90% confidence interval is shown for the Fe I line during eclipse. The red and blue lines indicate the best fit for constant and power-law models, respectively. The correlation coefficients, r , are as follows: $r = 0.82$, $r = 0.81$, and $r = 0.87$ for the Fe I, Fe XXV, and Fe XXVI lines, respectively. Using a logarithmic parameter space, we measured the slope of the Fe K α line flux vs. continuum flux— $m = 1.0 \pm 0.1$, $m = 0.6 \pm 0.1$, and $m = 0.7 \pm 0.1$ for the Fe I, Fe XXV, and Fe XXVI lines, respectively. The blue points indicate the data collected during eclipse.

(A color version of this figure is available in the online journal.)

combination of intrinsic and interstellar absorbers. According to our calculation, if $\sim 40\%$ of the measured fully covered N_H is intrinsic to the source and the rest interstellar, then the inferred $E(B - R)$ would be consistent with an F-type mass donor.

Finally, we considered the possibility that the apparent spectral type is affected by heating by the radiation of the X-ray source. We first calculated the flux of 4U 1210-64 using both *Suzaku* and the PCA. Out of eclipse, the flux of 4U 1210-64 was found to be $\sim 2 \times 10^{-10}$ erg cm $^{-2}$ s $^{-1}$ for the power-law model with a high-energy cutoff model in the *Suzaku* data. The flux in the PCA is reported in Table 5 ranging from $0.29 \pm 0.03 \times 10^{-10}$ erg cm $^{-2}$ s $^{-1}$ to $8.9 \pm 0.4 \times 10^{-10}$ erg cm $^{-2}$ s $^{-1}$. We converted the apparent magnitude in the *R* band (Masetti et al. 2009) into an optical flux using Bessell (1979). The optical flux in the *R* band was found to be 0.08 Jy, which can be converted to $\sim 2 \times 10^{-7}$ erg cm $^{-2}$ s $^{-1}$. The flux ratio F_X/F_{opt} was found to be $\sim 10^{-4}$, which is much smaller than what is observed in systems where irradiation is important (e.g., F_X/F_{opt} was found to be $\sim 10^2$ in Her X-1; Bradt & McClintock 1983). We conclude that irradiation effects are negligible in 4U 1210-64.

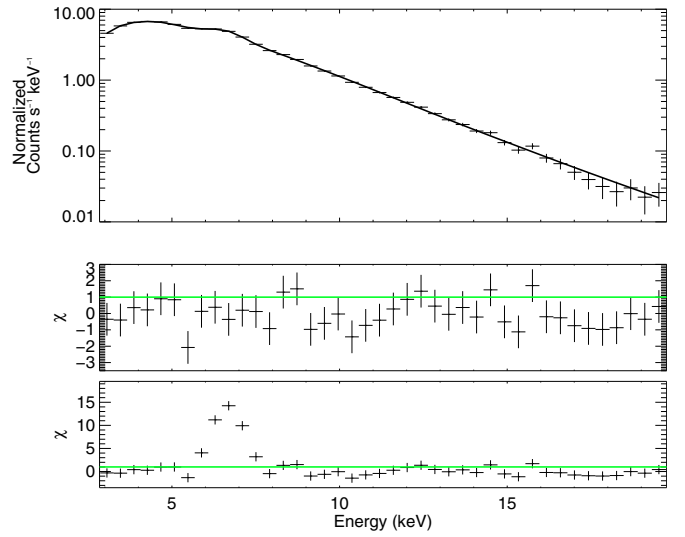


Figure 14. Typical PCA spectrum (MJD 54804) and best-fit model (top panel). This consists of a continuum comprised of a power law with a high-energy cutoff and a broad Fe K α emission line. Residuals of the best-fit model are plotted in the middle panel. To illustrate the Fe K α emission lines along with the best-fit model, the normalization of the line was set to zero. Residuals are plotted in the bottom panel.

(A color version of this figure is available in the online journal.)

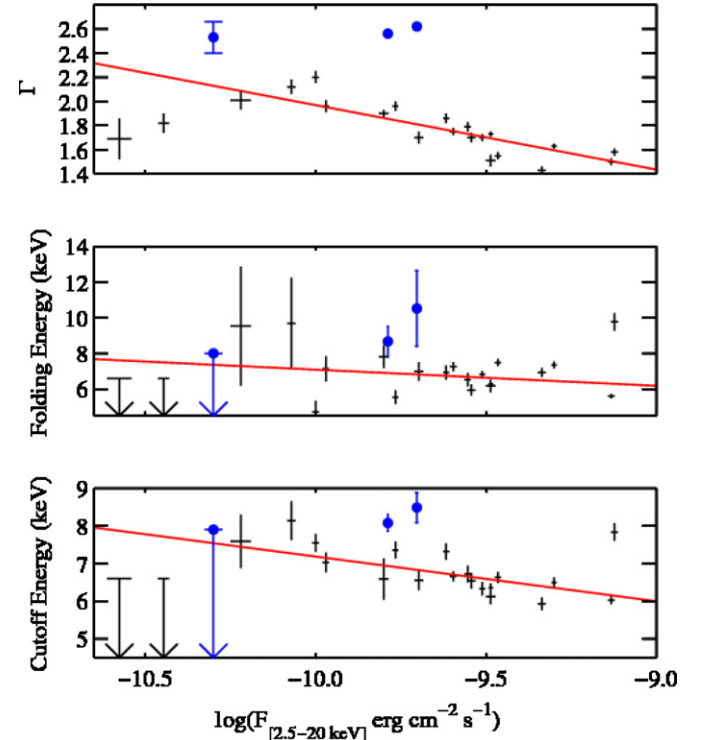


Figure 15. Power-law index (top), folding energy (middle), and cutoff energy (bottom) for the PCA spectra vs. the continuum flux in the 2.5–20 keV band in logarithmic units. The red lines indicate the best fit for the power-law model. The correlation coefficients (r) are: -0.72 and -0.80 for the high-energy cutoff and power-law index, respectively. The blue points indicate the data collected during eclipse.

(A color version of this figure is available in the online journal.)

4.1.3. Is 4U 1210-64 an Intermediate-mass X-Ray Binary?

In addition to the possibility that the donor star is a B-type giant, the duration of the eclipse suggests that an intermediate-mass classification cannot be ruled out. We found that the eclipse

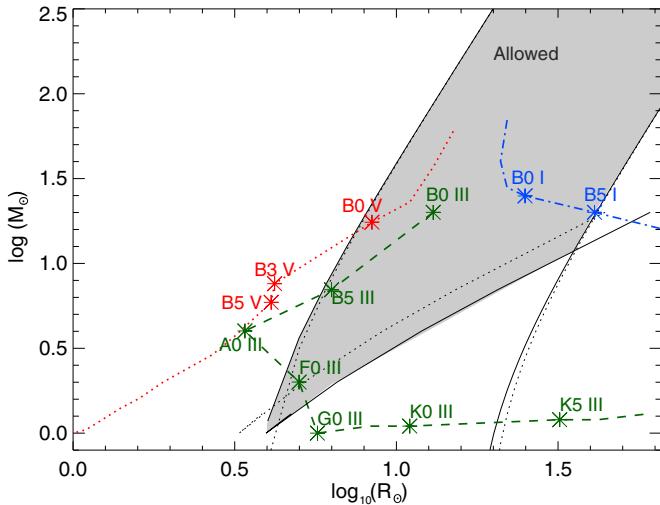


Figure 16. Log-log plot of stellar masses as a function of stellar radii. The shaded region, derived using Equation (E.4) in Chakrabarty (1996) for all possible inclination angles, indicates the allowed spectral types that satisfy the eclipse observed in the BAT, MAXI, and ASM folded light curves provided that the compact object is $1.4 M_{\odot}$ (see Figures 3 and 4, respectively). The black dotted lines show the allowed spectral types that satisfy the eclipse for a compact object of $1.9 M_{\odot}$ (see Section 4.1). Stellar masses and radii are given in Table 6. (A color version of this figure is available in the online journal.)

half-angle is consistent with F0 and G0 giants at inclination angles exceeding 79° and 70° , respectively (see Table 6). Using the values for M_V and A_R published in Carroll & Ostlie (2006) and Masetti et al. (2009), the distance of 4U 1210-64 was found to be ~ 0.9 kpc and ~ 1.3 kpc for a mass donor of spectral types F0 III and G0 III, respectively; which places 4U 1210-64 at a luminosity of $\sim 10^{34}$ erg s^{-1} (see Table 6). Other intermediate XRBs that host F-type stars include Cyg X-2 and Her X-1 (e.g., Seward & Charles 1995), which have considerably higher luminosities on the order of $\sim 10^{37}$ erg s^{-1} . The luminosities calculated for the F0 III and G0 III spectral types still exceed that of CVs (see Section 4.2).

The possibility that the mass donor in 4U 1210-64 is an intermediate or late-type star hints at the presence of an accretion disk. XRBs that host intermediate- and low-mass stars accrete matter through Roche-lobe overflow (see Equation (2); Eggleton 1983). The Roche lobe places an additional constraint on the spectral type of the mass donor in 4U 1210-64. While a spectral type of G0 III satisfies the observed eclipse half-angle, the Roche lobe would be significantly overfilled (see Table 6).

Finally, we discuss caveats in our hypothesis that the mass donor is an intermediate-mass star. No strong disk component was found, which is expected in the spectra of intermediate-mass X-ray binaries (e.g., Seward & Charles 1995). We note that the reddening, $E(B - R)$, was found to be consistent with main-sequence and giant B-type stars but was inconsistent with F-type and G-type stars (see Section 4.1.2). While $E(B - R)$ is apparently inconsistent with F-type stars, the possibility of systematic effects prevents excluding F-type stars as the possible mass donor (see Section 4.1.2). However, we can confidently exclude G-type stars due to the additional constraint that the Roche lobe is not significantly overfilled.

4.2. What is the Nature of the Compact Object?

The nature of the compact object present in 4U 1210-64 remains ambiguous. An analysis of the ASM, MAXI, and PCA power spectra shows that no pulsation period could be identified.

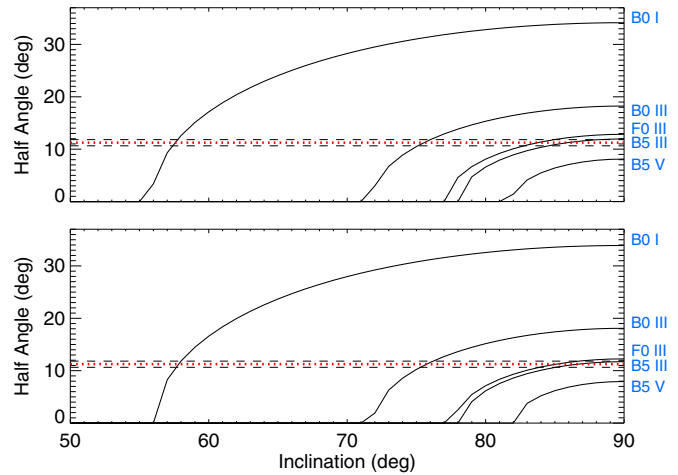


Figure 17. Black curves show the predicted eclipse half-angle as a function of inclination for stars with the indicated spectral types. The red and black dashed lines indicate the half-angle and its estimated error as measured by ASM and MAXI (see Section 4.1). We assume a neutron star mass of $1.4 M_{\odot}$ (top) and of mass $1.9 M_{\odot}$ (bottom) and typical masses and radii for the assumed companion spectral type (see Table 6).

(A color version of this figure is available in the online journal.)

The PCA power spectra, which cover the range of 860 s to 38 days (see Figure 9) and 10 ms–14 minutes (see Figure 10), are dominated by red noise, which could compromise our search for the pulsation period. While we removed the low-frequency noise from the power spectra (see Section 3.3.2), the PCA power spectrum covering the range of 860 s to 38 days was still compromised due to the orbital period of *RXTE* (see Figure 9). A pulsation period would provide a clear indication that the compact object is a neutron star. Spectral results thus far have also been inconclusive. Cyclotron lines, which would have proved a neutron star explanation for the compact object, are absent in the *Suzaku* spectra. Additionally, the *Suzaku* and PCA data suggest that the continuum can be modeled using an absorbed cutoff power law where the high-energy cutoff is 5.5 ± 0.2 keV. Since a firm identification of the nature of the compact object in 4U 1210-64 has proven elusive thus far, we compare our findings to systems where the compact object is known.

We first discuss the possible scenario that the compact object present in 4U 1210-64 is a black hole. Observations show that the exponential cut-off energy in HMXBs that host black holes exceeds 60 keV (Tomsick et al. 2009), sharply contrasting with the 5.5 ± 0.2 keV cut-off observed in the *Suzaku* spectra. Additionally, *INTEGRAL* observations reveal the presence of soft excess in 4U 1210-64 (Masetti et al. 2010), which is characteristic of HMXBs that host neutron stars (Hickox et al. 2004). The low high-energy cutoff suggests that a black hole explanation of the compact object is unlikely.

We also consider the possibility that the compact object could be an accreting white dwarf. The luminosities observed in CVs depend on the magnetic nature of the white dwarf, which affects the mode of accretion. The most luminous sub-type of CV, the intermediate polars, were found to be on the order of 10^{31} – 4×10^{33} erg s^{-1} (Brunschweiler et al. 2009). In comparison, the luminosities calculated for 4U 1210-64 exceed the above result by at least 1–2 orders of magnitude (see Table 6). Assuming a bremsstrahlung fit, Brunschweiler et al. (2009) found the temperatures (kT_{brems}) of intermediate polars are on the order of 10–40 keV, which differs from the value observed in 4U 1210-64 (see Section 3.4.1). Since a bremsstrahlung model was found

to be an unsatisfactory fit to the PCA data, we conclude that the CV explanation is unlikely.

Finally, we discuss the possibility that 4U 1210-64 contains a neutron star. Several geometries have been proposed to describe the apparent lack of a signal corresponding to the pulsation period. One possibility is a coalignment of the magnetic and spin axes of the neutron star (e.g., Bodaghee et al. 2010). A second explanation suggests that throughout the rotation the accretion beam points in our direction (e.g., Bodaghee et al. 2010). The absence of a well-defined pulsation period could also be explained by a weak magnetic field. Another possibility is that the compact object in 4U 1210-64 is a slowly rotating neutron star (e.g., 2S 0114+650; Farrell et al. 2008, and references therein).

4.3. What is the Physical Process Responsible for the Low State Observed in the ASM Data?

The ASM data reveal the presence of three distinct system states as previously noted by Corbet & Mukai (2008). These are two active states and one low state we interpret as quiescence (see Section 3.1.1). This long-term variability is suggestive of a variable accretion rate.

We first discuss the possibility that 4U 1210-64 is powered by the Be mechanism. In BeXBs the compact object accretes material from the circumstellar disk of a rapidly rotating main-sequence or giant B-type star. If the system is a BeXB, changes in the circumstellar disk around the Be star could also explain the period of low activity. Observations indicate that bright and faint states might correspond to the formation and dissipation of the circumstellar disk (Reig et al. 2010). The timescale for the development and disappearance of a circumstellar disk is typically on the order of 3–7 yr, which is consistent with the ASM data. One notable BeXB is SAX J2103.5+4545, which consists of a neutron star in a 12.7 day orbit around a B0Ve star (Reig et al. 2010). The timescale for the development and disappearance of the circumstellar disk is 1–2 yr, possibly due to the short orbital period (Reig et al. 2010). While a BeXB explanation supports the presence of high and low states observed in the ASM data, the presence of an eclipse of the compact object is inconsistent with most main-sequence B-type stars, where main-sequence stars later than a B0 do not satisfy the observed eclipse half-angle (see Figures 16 and 17). This is not surprising due to the smaller radius of the mass donors observed in most BeXBs. We note, however, that B-type giants would satisfy the observed eclipse duration at high inclination angles (see Section 4.1). Additionally, the Balmer lines, particularly the $H\alpha$ line, were found to be in absorption during Masetti et al.’s (2009) optical campaign of 4U 1210-64 (MJD 54529.3). Since Masetti’s observation occurred during a high state of the system (see Table 1 and Section 3.1.1), we would expect to see $H\alpha$ in emission (Silaj et al. 2010).

We also consider the possibility that the state transitions originate due to a mechanism similar to what is observed in black hole candidates (BHCs). Multiple states are observed in BHCs, which are defined as soft/high, intermediate, and hard/low (Cygnus X-1; GX 339-4, Grinberg et al. 2013; Nowak 2006; Dunn et al. 2010). The high-energy cutoff in BHCs exceeds 60 keV (Tomsick et al. 2009), which is in variance with our results obtained with *Suzaku* and PCA. Additionally, a disk blackbody is required to model the low-energy spectra of BHCs in the soft/high state (Shakura & Sunyaev 1973; Nowak 2006), which is not seen in the *Suzaku* and PCA analysis of 4U 1210-64.

Finally, we discuss the possibility that the mode of accretion in 4U 1210-64 is Roche lobe overflow, which primarily occurs in both intermediate and low-mass X-ray binaries. We compare the long-term behavior of 4U 1210-64 to that seen in soft X-ray transients, NS-LMXBs that host at least two different states (e.g., Aql X-1; Sakurai et al. 2013). In soft X-ray transients, the physical mechanism that could lead to a reduction of intensity is changes in the accretion rate, \dot{M} (Sakurai et al. 2013). The luminosity is significantly reduced when the accretion rate is low. Since the magnetic field of the majority of NS-LMXBs is weak, the propeller effect becomes important when the accretion rate, \dot{M} , is low (Sakurai et al. 2013). The long-term behavior of 4U 1210-64 differs from soft X-ray transients. While there are extended low states (Matsuoka & Asai 2013; Sakurai et al. 2013), the high states are shorter and brighter than what is observed in 4U 1210-64 (Coti Zelati et al. 2014).

No mechanisms described above appear to be consistent with 4U 1210-64. While there are uncertainties in the spectral classification, we note that the behavior of intermediate-mass X-ray binaries is not well known. Therefore, if 4U 1210-64 is a member of this class, unusual variability may be possible.

4.4. What is the Origin of the Variability in the High State?

Our analysis of the *Suzaku* and PCA data reveals the presence of strong variability in the light curves (see Figures 5 and 7). In the *Suzaku* data, “flares” were observed to reach nearly 1.4 times the mean count rate (i.e., a modulation depth of 140%). The variability is even stronger in the PCA data, where the modulation depth was found to be 330%. A reduced count rate was found in the PCA light curve between \sim MJD 54830–54833, which is outside the eclipse (see Figure 7). The unabsorbed flux of 4U 1210-64 was found to vary by a factor of \sim 25 over the course of both the *Suzaku* and PCA observations (see Sections 3.4.1 and 3.4.2).

The large variability in the *Suzaku* and PCA light curves could be attributed to several different physical processes, all resulting in changes in the accretion rate, \dot{M} . A positive correlation between the *Suzaku* hardness ratio and continuum flux was found (see Figure 6), which provides evidence against a strong wind. This is further strengthened by a decrease in the *Suzaku* hardness ratio during the egress phase of the observation. Since the system is eclipsing, a strong wind should lead to an increase in absorption and thus the X-ray hardness ratio during the ingress and egress phases of the orbit (Clark et al. 1988; Doroshenko et al. 2013; Suchy et al. 2008). The folded MAXI and ASM light curves (see Figure 18, top and bottom) provide additional evidence against it. The increase in the folded MAXI hardness ratio is modest (Figure 18, top), indicating the possible presence of a tenuous wind but not of a typical HMXB wind (e.g., Vela X-1; Cen X-3, Doroshenko et al. 2013; Suchy et al. 2008). Such behavior is not seen in the folded hardness ratio produced by the ASM, which is possibly due to the low count rate (see Figure 18, bottom). The observed N_H could possibly originate in an accretion stream (e.g., Cygnus X-1; Hanke et al. 2009, and references therein).

Magnetic and centrifugal barriers have been proposed to inhibit the accretion process in XRBs on hourly timescales (Bozzo et al. 2008), where the timescale is consistent with the variability in the light curve. This could explain the reduced count rate in the PCA light curve (see Figure 7, top). Another mechanism that could lead to such a reduction is the formation

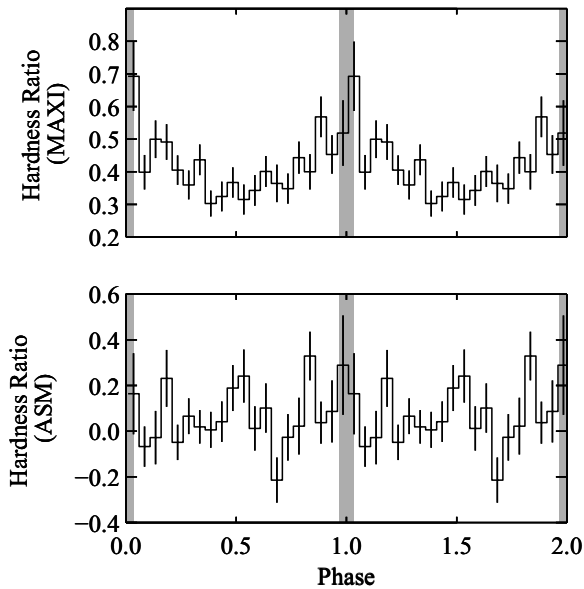


Figure 18. Hardness ratios of the folded MAXI (top) and ASM (bottom) light curves. The hardness ratio is defined as $C_{\text{hard}} - C_{\text{soft}} / C_{\text{hard}} + C_{\text{soft}}$, where the soft and hard energy bands are defined as 2–4 keV and 4–10 keV and 1.5–5 keV and 5–12 keV for the MAXI and ASM light curves, respectively. The eclipse is indicated by the shaded regions.

and dissipation of an unstable accretion disk (e.g., Bodaghee et al. 2011, and references therein).

4.5. Emission Lines

The analysis of spectral data produced by *Suzaku* reveals the presence of emission lines at energies of 2.6 keV, 6.4 keV, 6.7 keV, and 6.97 keV. We interpret the emission lines as S xvi K α , Fe K α , Fe xxv K α , and Fe xxvi K α , respectively. Below we discuss the mechanisms that are proposed to explain the emission lines seen in 4U 1210-64.

4.5.1. Fe K α Emission

A 6.4 keV emission line has been shown to be present in many XRBs (e.g., Vela X-1, 4U 1700-377, Cen X-3, and 4U 1822-37; Schulz et al. 2002; van der Meer et al. 2005; Naik et al. 2011; Sasano et al. 2013). The origin of the 6.4 keV emission line is due to neutral Fe or Fe in a low ionization state. Unless otherwise stated, we assume that Fe I emission is responsible for the 6.4 keV emission line.

Our analysis of the Fe I line indicates that the line flux tracks the flux in the continuum in the 7.1–9.0 keV band when 4U 1210-64 is out of eclipse and is not detected in eclipse (see Section 3.4.1). This is suggestive that the region responsible for the Fe I emission is close to the compact object. The accretion mechanism in 4U 1210-64 differs from the X-ray excited wind observed in the HMXB Cen X-3 (Day & Stevens 1993), but the Fe K α emission region is similar in both objects. For instance, the Fe I emission line in Cen X-3 was observed to be weakest during the eclipse phase (Ebisawa et al. 1996; Naik & Paul 2012). Because of these similarities, we compare 4U 1210-64 with Cen X-3 to understand the Fe K α emission feature.

Possible mechanisms that have been suggested to cause the fluorescence of cold material include a plasma layer at the surface of the Alfvén shell and an optically thick accretion disk (Basko 1980; Ebisawa et al. 1996). The flux of Fe I was found to decrease by more than an order of magnitude during

eclipse, which is comparable to the change of flux observed in the continuum. This is further indication that the origin of the Fe I emission is close to the compact object. The slope of the Fe I flux versus the continuum flux is near unity, which shows that the Fe I emission is in agreement with fluorescence (Nespoli et al. 2012; Reig & Nespoli 2013).

We also consider the mechanism responsible for the Fe xxv and Fe xxvi emission features. A possible correlation between the flux of both the Fe xxv and Fe xxvi emission features with respect to the continuum flux in the 7.1–9.0 keV band was found, which shows that the presence of Fe xxv and Fe xxvi increases as the continuum flux increases (see Section 3.4). We note that the slope between the continuum flux and the flux of the lines is significantly less than one, which we interpret as a possible sign that an increasing part of the medium might be completely ionized.

To place constraints on the state of the plasma, we analyzed the flux ratio between the Fe xxv and Fe xxvi emission features and the continuum flux in the 7.1–9.0 keV band. No change was found in the flux ratio between the Fe xxv and Fe xxvi emission features and the continuum flux in the 7.1–9.0 keV band (see Table 4), which indicates that the Fe xxv and Fe xxvi features possibly originate in the same region of a structured medium, where the ionization state can be independent of luminosity (Ebisawa et al. 1996), which is in agreement with our result of a constant flux ratio as a function of luminosity.

Fe xxvi and Fe xxv are likely due to photoionization. Recombination followed by electron cascade transitions is present in systems such as SMC X-1 (Vrtilek et al. 2001), Cen X-3 (Nespoli et al. 2012; Reig & Nespoli 2013), Vela X-1 (Goldstein et al. 2004), 4U 1700-37 (Liedahl & Paerels 1996), and 4U 1822-37 (Sasano et al. 2013). Emission features are more prominent during eclipse since direct emission from the compact object irradiating the accretion stream is no longer visible. The photoionization mechanism must originate in regions of low density since the range of luminosities we inferred in 4U 1210-64 (see Table 6) is significantly lower than what is observed in systems such as Cen X-3 and SMC X-1 ($\sim 10^{37}$ erg s $^{-1}$, Naik & Paul 2012; Vrtilek et al. 2001).

The very large EQWs of the Fe xxv and Fe xxvi emission features in eclipse (see Section 3.4) are consistent with an origin due to the reprocessing of photons in the accretion stream. In comparison, the EQW of the Fe xxv and Fe xxvi emission features observed in the HMXB Cen X-3 is largest during eclipse and tends to decrease as the continuum flux increases (Naik & Paul 2012). Naik & Paul (2012) show that the region responsible for the Fe xxv and Fe xxvi emission observed in Cen X-3 is extended and is comparable to the size of the mass donor in the system, which is likely what we observe in 4U 1210-64.

4.5.2. The Presence of S xvi in 4U 1210-64

Different ionization species of low to mid-Z elements such as S are present in eclipsing XRBs (e.g., Vela X-1, 4U 1700-377, and LMC X-4, Schulz et al. 2002; van der Meer et al. 2005; Hung et al. 2010). While near neutral fluorescent lines in addition to highly ionized species of emission lines were observed in SGXBs such as Vela X-1 (Schulz et al. 2002), the *Suzaku* spectra of 4U 1210-64 reveal only the highly ionized species of S xvi.

It has been shown that photoionization and radiative recombination are responsible for the presence of hydrogen-like species of S in absorbed XRBs (Iaria et al. 2004). The S xvi K α emission features only appeared during part of the *Suzaku* observation

(see Table 4). As a result, we could not measure the temporal variability of the EQW or fluxes of S XVI.

5. CONCLUSION

4U 1210-64, for which we determined an orbital period of 6.7101 ± 0.0005 days, is a unique XRB. The companion star was previously proposed to have a spectral type of B5 V. We found that a B5 V classification does not satisfy the eclipse half-angle, compelling evidence against a B5 V classification. 4U 1210-64s spectral features seem to indicate that the mass donor could be a B0 V or B0-5 III star. A Be-type accretion mechanism, with most BeXBs hosting primaries of spectral type late O to B2 (Negueruela 1998), is unlikely, since these systems usually have longer periods and are transients. A supergiant classification must be excluded since the implied distance would put the object outside the Galaxy. F-type giants also satisfy the constraints imposed by the eclipse half-angle and Lagrange point, L1, where Roche-lobe transfer would be expected to occur. To further constrain the spectral type of the mass donor, the reddening values $E(B - R)$ were calculated for the possible spectral types. The reddening was found to be consistent with main-sequence and giant B-type stars but was inconsistent with F-types. Due to the uncertainties in the conversion between the N_H and $E(B - R)$, we cannot completely exclude an F-type mass donor.

4U 1210-64 hosts a compact object that remains ambiguous in nature. No signs of pulsations or cyclotron features were found in our analysis of 4U 1210-64, which would prove that the compact object is a neutron star. The spectral properties of the continuum strongly contrast with those typically seen in BHCs as well as CVs. In particular, a disk blackbody is required to model the low-energy spectra of BHCs in the soft/high state while CVs are typically fit with a bremsstrahlung model. While the nature of the compact object has proven elusive, a neutron star with a weak magnetic field possibly aligned with the spin axis is consistent with the lack of pulsations and cyclotron features.

Emission lines at 2.62 keV, 6.41 keV, 6.7 keV, and 6.97 keV were all clearly detected in the *Suzaku* spectra, which we interpret as S XVI $K\alpha$, Fe $K\alpha$, Fe XXV $K\alpha$, and Fe XXVI $K\alpha$, respectively. The flux of the Fe $K\alpha$ lines closely tracks the flux of the unabsorbed continuum. We found a linear relationship between the flux of Fe I versus the continuum, which shows that the most probable origin of the Fe I line is fluorescence of cold and dense material close to the compact object. An origin close to the compact object is further supported by the fact that Fe I is not clearly detected during eclipse. The slopes of the relationship between the logarithm of the Fe XXV and Fe XXVI flux versus the logarithm continuum possibly show that an increasing part of the medium might be completely ionized as the flux increases.

Strong variability was found in the *Suzaku* and PCA observations. The out-of-eclipse flux was found to be $1.73^{+0.06}_{-0.05} \times 10^{-10} \text{ erg s}^{-1} \text{ cm}^{-2}$, which implies a luminosity of $\sim 10^{34-36} \text{ erg s}^{-1}$. The variability was found to be a factor of 25 in both the *Suzaku* and PCA observations. A positive correlation was seen in both the *Suzaku* hardness–intensity diagram and the PCA color–color diagram, which provides evidence against a strong wind. In eclipsing XRBs, a strong wind should lead to an increase in absorption and thus the X-ray hardness ratio during the ingress and egress phases of the orbit. Additional evidence from the folded MAXI and ASM light curves suggests that the observed N_H could originate possibly originate in an accretion stream.

4U 1210-64 appears to be an NS-HMXB but conclusive evidence remains to be found. Additional multi-wavelength observations are required to achieve a full understanding of the source.

We thank Drs. Tim Kallman, Vanessa McBride, and Joern Wilms for useful discussion. We also thank the anonymous referee for useful comments.

REFERENCES

- Allen, K. W. (ed.) 2000, in *Astrophysical Quantities* (Translated from the 4th Revised and Suppl. English edition; Moskva: Mir), 448
- Audley, M. D., Nagase, F., Mitsuda, K., Angelini, L., & Kelley, R. L. 2006, *MNRAS*, **367**, 1147
- Balucinska-Church, M., & McCammon, D. 1992, *ApJ*, **400**, 699
- Barlow, E. J., Knigge, C., Bird, A. J., et al. 2006, *MNRAS*, **372**, 224
- Barthelmy, S. D., Barbier, L. M., Cummings, J. R., et al. 2005, *SSRv*, **120**, 143
- Basko, M. M. 1980, *A&A*, **87**, 330
- Bessell, M. S. 1979, *PASP*, **91**, 589
- Bevington, P. R., & Robinson, D. K. (ed.) 2003, *Data Reduction and Error Analysis for the Physical Sciences* (3rd ed.; Boston, MA: McGraw-Hill)
- Bodaghee, A., Tomsick, J. A., Rodriguez, J., et al. 2010, *ApJ*, **719**, 451
- Bodaghee, A., Tomsick, J. A., Rodriguez, J., et al. 2011, *ApJ*, **727**, 59
- Boldt, E. 1987, in *IAU Symp. 124, Observational Cosmology*, ed. A. Hewitt et al. (Dordrecht: D. Reidel), 611
- Bozzo, E., Falanga, M., & Stella, L. 2008, *ApJ*, **683**, 1031
- Bradt, H. V. D., & McClintock, J. E. 1983, *ARA&A*, **21**, 13
- Brunschweiler, J., Greiner, J., Ajello, M., & Osborne, J. 2009, *A&A*, **496**, 121
- Burrows, D. N., Hill, J. E., Nousek, J. A., et al. 2005, *SSRv*, **120**, 165
- Carroll, B. W., & Ostlie, D. A. 2006, *An Introduction to Modern Stellar Astrophysics* (Reading, MA: Institute for Mathematics and Its Applications)
- Chakraborty, D. 1996, PhD thesis, California Institute of Technology
- Clark, G. W., Minato, J. R., & Mi, G. 1988, *ApJ*, **324**, 974
- Corbet, R. H. D., & Mukai, K. 2008, *ATel*, **1861**, 1
- Coti Zelati, F., Campana, S., D’Avanzo, P., & Melandri, A. 2014, *MNRAS*, **438**, 2634
- Cusumano, G., La Parola, V., Segreto, A., et al. 2010, *A&A*, **510**, A48
- Day, C. S. R., & Stevens, I. R. 1993, *ApJ*, **403**, 322
- Day, C. S. R., & Tennant, A. F. 1991, *MNRAS*, **251**, 76
- Dickey, J. M., & Lockman, F. J. 1990, *ARA&A*, **28**, 215
- Doroshenko, V., Santangelo, A., Nakahira, S., et al. 2013, *A&A*, **554**, A37
- Dunn, R. J. H., Fender, R. P., Körding, E. G., Belloni, T., & Cabanac, C. 2010, *MNRAS*, **403**, 61
- Ebisawa, K., Day, C. S. R., Kallman, T. R., et al. 1996, *PASJ*, **48**, 425
- Eggleton, P. P. 1983, *ApJ*, **268**, 368
- Elvis, M., Plummer, D., Schachter, J., & Fabbiano, G. 1992, *ApJS*, **80**, 257
- Farrell, S. A., Sood, R. K., O’Neill, P. M., & Dieters, S. 2008, *MNRAS*, **389**, 608
- Forman, W., Jones, C., Cominsky, L., et al. 1978, *ApJS*, **38**, 357
- Foster, A. R., Ji, L., Smith, R. K., & Brickhouse, N. S. 2012, *ApJ*, **756**, 128
- Goldstein, G., Huenemoerder, D. P., & Blank, D. 2004, *AJ*, **127**, 2310
- Gray, R. O., & Corbally, C. J. 2009, in *Stellar Spectral Classification*, ed. R. O. Gray & C. J. Corbally (Princeton, NJ: Princeton Univ. Press), 122
- Grinberg, V., Hell, N., Pottschmidt, K., et al. 2013, *A&A*, **554**, A88
- Güver, T., & Oumlzel, F. 2009, *MNRAS*, **400**, 2050
- Hanke, M., Wilms, J., Nowak, M. A., et al. 2009, *ApJ*, **690**, 330
- Hickox, R. C., Narayan, R., & Kallman, T. R. 2004, *ApJ*, **614**, 881
- Hung, L.-W., Hickox, R. C., Boroson, B. S., & Vrtillek, S. D. 2010, *ApJ*, **720**, 1202
- Iaria, R., Di Salvo, T., Robba, N. R., et al. 2004, *ApJ*, **600**, 358
- Jahoda, K., Markwardt, C. B., Radeva, Y., et al. 2006, *ApJS*, **163**, 401
- Jahoda, K., Swank, J. H., Giles, A. B., et al. 1996, *Proc. SPIE*, **2808**, 59
- Kalberla, P. M. W., Burton, W. B., Hartmann, D., et al. 2005, *A&A*, **440**, 775
- Koyama, K., Tsunemi, H., Dotani, T., et al. 2007, *PASJ*, **59**, 23
- Krimm, H. A., Holland, S. T., Corbet, R. H. D., et al. 2013, *ApJS*, **209**, 14
- Lattimer, J. M. 2012, *ARNPS*, **62**, 485
- Levine, A. M., Bradt, H., Cui, W., et al. 1996, *ApJL*, **469**, L33
- Liedahl, D. A., & Paerels, F. 1996, *ApJL*, **468**, L33
- Masetti, N., Landi, R., Sguera, V., et al. 2010, *A&A*, **511**, A48
- Masetti, N., Parisi, P., Palazzi, E., et al. 2009, *A&A*, **495**, 121
- Matsuoka, M., & Asai, K. 2013, *PASJ*, **65**, 26
- Matsuoka, M., Mihara, T., Sugizaki, M., et al. 2010, *Proc. SPIE*, **7732**, 77320Y
- Mitsuda, K., Bautz, M., Inoue, H., et al. 2007, *PASJ*, **59**, 1
- Naik, S., & Paul, B. 2012, *BASI*, **40**, 503

- Naik, S., Paul, B., & Ali, Z. 2011, [ApJ](#), **737**, 79
- Negueruela, I. 1998, [A&A](#), **338**, 505
- Nespoli, E., Reig, P., & Zezas, A. 2012, [A&A](#), **547**, A103
- Nowak, M. A. 2006, in Proc. VI Microquasar Workshop: Microquasars and Beyond, ed. B. Tomaso (POS), **1.1**
- Nowak, M. A., Hanke, M., Trowbridge, S. N., et al. 2011, [ApJ](#), **728**, 13
- Predehl, P., & Schmitt, J. H. M. M. 1995, [A&A](#), **293**, 889
- Reig, P., & Nespoli, E. 2013, [A&A](#), **551**, A1
- Reig, P., Słowińska, A., Zezas, A., & Blay, P. 2010, [MNRAS](#), **401**, 55
- Remillard, R. A., & Levine, A. M. 1997, in All-Sky X-Ray Observations in the Next Decade, ed. M. Matsuoka & N. Kawai (Japan: RIKEN), 29
- Revnivtsev, M., Sazonov, S., Krivonos, R., Ritter, H., & Sunyaev, R. 2008, [A&A](#), **489**, 1121
- Revnivtsev, M., Sunyaev, R., Lutovinov, A., & Sazonov, S. 2007, [ATel](#), **1253**, 1
- Reynolds, A. P., Parmar, A. N., Hakala, P. J., et al. 1999, [A&AS](#), **134**, 287
- Rieke, G. H., & Lebofsky, M. J. 1985, [ApJ](#), **288**, 618
- Sakurai, S., Torii, S., Noda, H., et al. 2013, [PASJ](#), **66**, 10
- Sasano, M., Makishima, K., Sakurai, S., Zhang, Z., & Enoto, T. 2013, [PASJ](#), **66**, 35
- Scargle, J. D. 1982, [ApJ](#), **263**, 835
- Schulz, N. S., Canizares, C. R., Lee, J. C., & Sako, M. 2002, [ApJL](#), **564**, L21
- Seward, F. D., & Charles, P. A. (ed.) 1995, *Exploring the X-Ray Universe* (Cambridge: Cambridge Univ. Press)
- Shakura, N. I., & Sunyaev, R. A. 1973, [A&A](#), **24**, 337
- Silaj, J., Jones, C. E., Tycner, C., Sigut, T. A. A., & Smith, A. D. 2010, [ApJS](#), **187**, 228
- Suchy, S., Pottschmidt, K., Wilms, J., et al. 2008, [ApJ](#), **675**, 1487
- Takahashi, T., Abe, K., Endo, M., et al. 2007, [PASJ](#), **59**, 35
- Tomsick, J. A., Chaty, S., Rodriguez, J., et al. 2009, [ApJ](#), **694**, 344
- Tueller, J., Baumgartner, W. H., Markwardt, C. B., et al. 2010, [ApJS](#), **186**, 378
- Ubertini, P., Lebrun, F., Di Cocco, G., et al. 2003, [A&A](#), **411**, L131
- van der Meer, A., Kaper, L., di Salvo, T., et al. 2005, [A&A](#), **432**, 999
- Vaughan, S. 2005, [A&A](#), **431**, 391
- Verrecchia, F., in't Zand, J. J. M., Giommi, P., et al. 2007, [A&A](#), **472**, 705
- Vrtilek, S. D., Raymond, J. C., Boroson, B., et al. 2001, [ApJL](#), **563**, L139
- Watanabe, S., Sako, M., Ishida, M., et al. 2006, [ApJ](#), **651**, 421
- Wegner, W. 1994, [MNRAS](#), **270**, 229
- Wilms, J., Allen, A., & McCray, R. 2000, [ApJ](#), **542**, 914
- Woo, J. W., Clark, G. W., Day, C. S. R., Nagase, F., & Takeshima, T. 1994, [ApJL](#), **436**, L5